INTERNATIONAL
Agrophysics
www.international-agrophysics.org

Int. Agrophys., 2026, 40, 255-276
doi: 10.31545/intagr/217982

Enhancing agricultural drought monitoring in semi-arid regions using spatiotemporal image fusion and a comprehensive agricultural drought index**

Masoume Nabavizadeh[1], *Iman Rousta*[1,2]*, *Kamal Omidvar*[1], *Haraldur Olafsson*[2], *Jaromir Krzyszczak*[3]*

[1]Department of Geography, Yazd University, Yazd 8915818411, Iran
[2]Institute for Atmospheric Sciences-Weather and Climate and Department of Physics, University of Iceland and Icelandic Meteorological Office (IMO), Bustadavegur 7, IS-108 Reykjavik, Iceland
[3]Institute of Agrophysics, Polish Academy of Sciences, Doświadczalna 4, 20-290 Lublin, Poland

Received October 16, 2025; accepted February 10, 2026

Abstract. Effective agricultural drought monitoring requires data with both high spatial and temporal resolution to capture rapid vegetation dynamics at the field scale, while current satellite systems rarely provide both simultaneously. This study addresses this limitation by applying a spatiotemporal data fusion and developing a robust agricultural drought index (ADI). The spatial-temporal image fusion model (STI-FM) was used to fuse moderate resolution imaging spectroradiometer (MODIS) and Landsat-8 data over Iranshahr County, southeastern Iran, producing high-temporal-resolution synthetic Landsat-8 imagery. A novel ADI was then developed by integrating uncorrelated drought-related indicators (normalized difference water index (NDWI), visible and shortwave infrared drought index (VSDI), temperature vegetation dryness index (TVDI), and land surface temperature (LST)), with TVDI included to enhance sensitivity to soil moisture and thermal stress in semi-arid fields. The fused images showed strong agreement with observed Landsat data, confirming reliable reconstruction of spectral and thermal patterns in agricultural areas. ADI-based drought assessment revealed persistent drought conditions during the 2014-2018 growing seasons (April-June). Comparisons with meteorological and hydrological drought indices showed consistent drought patterns, confirming the robustness and applicability of the proposed framework.

Keywords: agricultural drought, agricultural drought index (ADI), image fusion, Iranshahr, remote sensing

1. INTRODUCTION

Few natural hazards cut across borders, economies, and ecosystems as silently yet destructively as drought. Unlike floods or storms, drought develops gradually and often remains unnoticed until its impacts become severe, leading to reduced crop yields, increased wildfire risk, declining water supplies, and degradation of freshwater ecosystems. Rather than a simple rainfall deficit, drought reflects a sustained shortfall in water availability-in soils, rivers, reservoirs, or aquifers-relative to multi-decadal norms (McKee *et al.*, 1993; Mishra and Singh, 2010). Because of its inherently local character, the impacts vary substantially across regions. For instance, a two-month dry spell in the humid U.S. Midwest may cause limited economic consequences, whereas a similar deficit in rain-fed farms of the Sahel can trigger severe food insecurity. Understanding drought patterns is therefore essential for effective agricultural risk management and mitigation planning (Gholinia *et al.,* 2024; McKee *et al.*, 1993; Mishra and Singh, 2010).

In response, national and international agencies have developed and expanded monitoring networks that integrate meteorological observations (precipitation, temperature, wind speed, evapotranspiration) with hydrological data, *in-situ* soil moisture measurements, and socio-economic indicators such as crop yields or water use. Despite this

---

*Corresponding author e-mail: irousta@yazd.ac.ir
j.krzyszczak@ipan.lublin.pl

**This work was supported by Vedurfelagid, Rannis and Rannsoknastofa i vedurfraedi.

© 2026 Authors. Published by Institute of Agrophysics, Polish Academy of Sciences. This is an open access article licensed under the Creative Commons Attribution 4.0 License (CC BY 4.0)

integrative intent, most operational agricultural drought monitoring remains largely dominated by meteorological metrics, reflecting the long-term availability and spatial coverage of weather-station networks compared with the more spatially fragmented coverage of soil-moisture sensors or crop-stress observations (Meng *et al.*, 2025a; Wei *et al.*, 2024; Zargar *et al.*, 2011). While precipitation- and temperature-based indices are useful for early warnings of emerging water deficits, they often fail to capture the fine-scale heterogeneity of soil-moisture depletion and the actual physiological stress experienced by crops. Among the most widely applied indices are the standardized precipitation index (SPI), the Palmer drought severity index (PDSI), and the crop moisture index (CMI). The PDSI employs a two-layer water-balance model that integrates precipitation, temperature, and soil-moisture recharge to quantify cumulative moisture departures over multi-month intervals. The CMI, derived from the PDSI, isolates short-term surface-soil moisture anomalies within one- to two-month intervals and is more responsive during the growing season, though it can be unstable for agricultural applications. The SPI, in contrast, relies solely on precipitation data and can be computed over flexible time scales, from one month, useful for detecting rapid agricultural drought onset, to two years or more, reflecting extended hydrological deficits, enabling comparisons across regions and drought types. However, the SPI may underestimate drought severity during periods of elevated temperature-driven evaporation (Palmer, 1965, 1968; Poudel *et al.,* 2024; McKee *et al.*, 1993).

Traditional drought-monitoring approaches, although widely used, are inherently limited by their dependence on ground-based meteorological observations, which often lack the spatial resolution required to capture field-scale variability in soil moisture and crop stress. This limitation has increased the relevance of remote sensing and spatiotemporal data fusion techniques, particularly in data-scarce regions, where they provide continuous and spatially explicit observations that complement station-based monitoring frameworks (Gholinia *et al.,* 2024; Han *et al.*, 2020). Current satellite platforms offer a wide range of optical and thermal products for agricultural drought monitoring, but they differ substantially in spatial and temporal resolution. Sensors such as the moderate resolution imaging spectroradiometer (MODIS), the advanced very high resolution radiometer (AVHRR), the Suomi National Polar-orbiting Partnership Visible Infrared Imaging Radiometer Suite (NPP/VIIRS), and the Satellite Pour l'Observation de la Terre – Végétation (SPOT-VGT) provide frequent observations (daily to near-daily) at coarse spatial resolutions (250-1 000 m), whereas platforms such as Landsat, the advanced spaceborne thermal emission and reflection radiometer (ASTER), and the Satellite pour l'Observation de la Terre 5 (SPOT5) deliver finer spatial detail (10-120 m) at much lower temporal frequencies (16-26 days). Effective agricultural drought monitoring, however, requires both high spatial and temporal resolution due to the small size of cultivated fields and rapid vegetation dynamics during the growing season (Atzberger, 2013; Becker-Reshef *et al.*, 2010; Rocha *et al.*, 2012). While high spatial resolution is essential for field-scale analysis (Roy *et al.*, 2015), frequent observations are needed to capture short-term variations in vegetation condition associated with drought stress (Kovalskyy *et al.*, 2012; Wang and Qu, 2009; Zhang *et al.*, 2003). No operational satellite system currently satisfies both requirements simultaneously, owing to technical and cost constraints (Jiang *et al.*, 2011; Yang *et al.*, 2010).

To overcome this limitation, multi-sensor data fusion techniques have been developed to integrate complementary satellite observations and generate imagery with both high spatial and temporal resolution (Jia *et al.*, 2025; Jiang *et al.*, 2011; Lian *et al.*, 2026; Sun *et al.*, 2026; Yang *et al.*, 2010). Some recent methods further extend this concept by integrating multi-source remote sensing data with meteorological measurements and ancillary geospatial information within ensemble learning frameworks (Wang *et al.*, 2026). In general, image fusion combines information from multiple images of the same scene to enhance interpretation or quantitative analysis (Goshtasby and Nikolov, 2007; Qian *et al.*, 2025; Wang *et al.*, 2024; Zhang *et al.*, 2025). One of the earliest and most widely adopted spatiotemporal data fusion (STDF) models is the spatial and temporal adaptive reflectance fusion model (STARFM), introduced by Gao *et al.* (2006), which merges Landsat and MODIS surface reflectance data to predict high-resolution imagery at unsampled dates. Despite its usefulness, STARFM is limited by fixed window sizes, challenges in identifying spectrally similar pixels, and reduced accuracy in heterogeneous landscapes. Numerous extensions have been proposed to address these shortcomings (Fu *et al.*, 2013; Roy *et al.*, 2008; Zhu *et al.*, 2010; Zurita-Milla *et al.*, 2009; Meng *et al.*, 2013). For example, Zhu *et al.* (2010) developed the Enhanced STARFM (ESTARFM), which incorporates multiple Landsat-MODIS image pairs and applies linear regression to improve performance under complex land-cover conditions (Fu *et al.*, 2013), albeit at the cost of increased computational complexity and parameter dependence. The modified ESTARFM (mESTARFM) further refines pixel selection criteria to improve prediction reliability but remains computationally intensive (Fu *et al.*, 2013). Other adaptations incorporate domain-specific information, such as crop phenology (Spatial and Temporal Adaptive Vegetation index Fusion Model STAVFM; Meng *et al.*, 2013), annual thermal cycles for land surface temperature estimation (Spatio-temporal Adaptive Data Fusion Algorithm for Temperature mapping SADFAT; Weng *et al.*, 2014), or combining single-band and multi-band predictions (Single-band and Multi-band Spatiotemporal Fusion Model SMSTFM; Wang *et al.*, 2023). While these approaches improve performance for specific variables (*e.g.*, NDVI or LST), they still struggle in highly dynamic or heterogeneous environments (Meng *et al.*, 2013; Wang and Qu, 2009).

An alternative class of methods relies on spectral unmixing techniques. For example, Zurita-Milla *et al.* (2009) combined coarse-resolution MEdium Resolution Imaging Spectrometer (MERIS) time series with high-resolution Landsat-based land-use maps using linear mixing models, while Zhang (2008) proposed the ESTDFM model approach based on Iterative Self-Organizing Data Analysis Technique (ISODATA) classification and endmember analysis. Although capable of producing high-resolution outputs, these methods depend heavily on accurate land-cover information and are computationally demanding. Moreover, like STARFM-based models, they face limitations in reconstructing historical conditions. To address these limitations, Huang *et al.* (2012) proposed the Sparse-Representation-Based Spatiotemporal Fusion Model (SPSTFM), which employs sparse dictionary learning to model temporal reflectance changes. A subsequent enhancement using high-pass modulation reduced input data requirements and improved efficiency (Song and Huang, 2012). Nonetheless, the dictionary training process remains computationally expensive, limiting large-scale or operational applications.

Previously developed satellite image fusion techniques (Table 1) are often complex, computationally demanding, and time-consuming. To address these shortcomings, more recent approaches, such as the spatial-temporal image fusion model (STI-FM), have been proposed (Hazaymeh and Hassan, 2015). STI-FM offers a robust and efficient framework for reconstructing high-resolution imagery at frequent temporal intervals by integrating the temporal frequency of coarse-resolution sensors (*e.g.*, MODIS) with the spatial detail of higher-resolution platforms (*e.g.*, Landsat). The model generates synthetic imagery with high

Table 1. Overview of previously developed spatiotemporal data fusion models, highlighting their inputs, methodologies, strengths and limitations

Model	Inputs	Core method / Approach	Strengths	Limitations	Reference
STARFM	$L(t_1)$, $M(t_1)$, $M(t_2)$	Spectral similarity, weighting, fusion	Simple, widely used	Fixed window size, spectral mismatch, not robust in heterogeneous areas	Gao *et al.*, 2006
ESTARFM	$L(t_1)$, $L(t_3)$, $M(t_1)$, $M(t_2)$, $M(t_3)$	Linear regression between similar pixels	Improved accuracy over STARFM	Computationally intensive, still suffers from spectral similarity issues	Zhu *et al.*, 2010
MESTARFM	Same as ESTARFM	Adds conditions on spectral variance and vegetation type	Higher prediction accuracy	Long computation time	Fu *et al.*, 2013
STAVFM	Same as STARFM	Adds temporal weighting based on crop growth patterns	Improves NDVI prediction in agricultural regions	Limited to dominant agricultural land types	Meng *et al.*, 2013
SADFAT	Same as STARFM	Incorporates annual thermal cycles + spectral unmixing	Better LST prediction	Requires manual tuning of land cover and window	Wang and Qu, 2009
Unmixing	MERIS time series + high-res land use	Linear mixing model with pixel assignment	Accurate if land-use maps are good	Heavily dependent on external land-use data, expensive	Zurita-Milla *et al.*, 2009
ESTDFM	$L(t_1)$, $L(t_3)$, $M(t_1\text{-}t_3)$	ISODATA classification, endmember unmixing	Enables reconstruction using MODIS differences	Needs land-use maps, limited for past conditions	Zhang, 2008
SPSTFM	$L(t_1)$, $L(t_3)$, $M(t_1\text{-}t_3)$	Sparse dictionary learning + resampling	Higher accuracy than STARFM	Training dictionary is time-consuming	Huang *et al.*, 2013
SPSTFM-modified	$L(t_1)$, $M(t_1)$, $M(t_2)$	High-pass modulation + sparse transfer images	Fewer inputs, avoids past condition reconstruction	Still time-consuming	Song and Huang, 2012
STIFM	$L(t_1)$, $M(t_1\text{-}t_2)$	Sparse representation + temporal regularization	High accuracy, adaptive, low computational cost, no need for land-use data	–	Hazaymeh and Hassan, 2015

spatial (~30 m) and temporal (~8-day) resolution, enabling continuous monitoring of vegetation dynamics and drought processes at finer spatial scales. Based on sparse representation principles, STI-FM incorporates temporal regularization and adaptive dictionary learning, reducing input data requirements while improving performance in heterogeneous landscapes and maintaining temporal consistency across image time series (Chen *et al.*, 2025; Jia *et al.*, 2024). Comparative studies have demonstrated that STI-FM outperforms earlier fusion models, including STARFM, SPSTFM, and unmixing-based approaches, in reconstructing spectral bands while mitigating key limitations such as fixed spatial windows, spectral mismatch, reliance on auxiliary datasets, and high computational cost (Hazaymeh and Almagbile, 2018; Wang *et al.*, 2023). Furthermore, its adaptive framework supports the generation of high-frequency NDVI and other vegetation index time series, enhancing soil moisture estimation and drought detection during dry periods (Liao *et al.*, 2017). Overall, STI-FM provides a robust and efficient tool for agricultural drought monitoring, especially in heterogeneous and semi-arid environments.

Semi-arid regions are among the most vulnerable agroecosystems due to limited and highly variable rainfall, shallow soil moisture reserves, and fragile vegetation cover. These conditions complicate drought monitoring because of sparse canopy cover, strong soil-background effects, and rapid environmental variability (Huang *et al.*, 2025; Liu *et al.*, 2025; Peng *et al.*, 2025). In addition, wide spacing of meteorological stations, limited historical observations, and large spatial extents reduce the reliability of conventional ground-based assessments (Abu Arra and Şişman, 2024; Sun *et al.*, 2013; Xu *et al.*, 2023). Consequently, there is a clear need for monitoring approaches that provide high spatial resolution, frequent temporal coverage, and consistent observations to support reliable drought assessment and sustainable land and water management (Mliyeh *et al.,* 2025).

The primary objective of this study is to implement and evaluate the STI-FM technique in a semi-arid agricultural region in southeastern Iran (Iranshahr), where sparse ground observations and limited long-term data constrain traditional drought analyses. To address these challenges, a modified remote sensing-based index, the agricultural drought index (ADI), was applied to fused Landsat and MODIS images. The fusion model applied in this study follows the approach of Hazaymeh and Hassan (2015) but introduces a key modification: the integration of the temperature vegetation dryness index (TVDI). TVDI was selected because of its high sensitivity to moisture stress at fine spatial scales, which enhances drought detection in small and relatively homogeneous semi-arid areas. Its effectiveness under such conditions-particularly where air temperature variability and surface heterogeneity are limited-has been demonstrated in previous studies (Kimura, 2007; Rahimzadeh-Bajgiran *et al.*, 2012). Although research on the ADI remains limited, existing studies indicate strong potential for drought monitoring in semi-arid agricultural regions. By integrating multi-source, multi-variable indicators, the ADI has been shown to assemble the advantages of traditional single-variable drought indices and to perform reliably across diverse environmental conditions (Wang *et al.*, 2018; Rahman *et al.*, 2024). Comparative analyses further confirm its robustness, supporting its application in this study (Hamarash *et al.*, 2024; Sharafi and Ghaleni, 2023). Unlike widely applied composite indices such as the vegetation health index (VHI), which combines vegetation greenness (vegetation condition index, VCI) and thermal stress (thermal condition index, TCI) derived from NDVI and land surface temperature to infer vegetation condition (Gholinia *et al.,* 2024), the ADI adopted in this study is designed to explicitly represent multiple biophysical components of agricultural drought. While VHI primarily reflects vegetation responses to combined greenness and temperature stress, it does not directly account for soil moisture constraints or variations in vegetation water content, which are critical drivers of crop stress in semi-arid and irrigated systems. The ADI extends beyond vegetation-temperature coupling by integrating independent indicators of vegetation water status (NDWI), vegetation stress (VSDI), soil moisture conditions (TVDI), and surface energy balance (LST). In addition, the ADI employs a dynamic, scene-specific thresholding strategy, in which drought conditions are defined relative to the statistical distribution of each indicator within each 8-day composite, rather than using fixed or climatological thresholds commonly applied in indices. This adaptive formulation enhances sensitivity to short-term drought anomalies, local heterogeneity, and irrigation effects, which can decouple vegetation condition from precipitation and temperature signals.

Iranshahr was selected as a case study because it represents a highly drought-sensitive environment characterized by extreme heat, scarce rainfall, and dependence on fragile water and vegetation systems. Such regions require fine-scale, high-frequency monitoring, as small changes in soil moisture or vegetation cover can rapidly translate into agricultural losses. However, most commonly used drought indices rely on satellite data with either coarse spatial resolution or infrequent revisit times, limiting their ability to capture localized and rapidly evolving vegetation stress. Coarse-resolution products tend to smooth field-scale variability, while sensors with long revisit intervals may miss short-term processes such as rapid soil drying or transient vegetation recovery. Moreover, widely used optical indices (*e.g.*, VCI, TCI, VHI) are often further constrained by cloud contamination and spectral limitations (Liao *et al.*, 2017). By applying STI-FM for the Iranshahr region, this study addresses a key methodological gap by combining spatial detail with temporal responsiveness. The resulting fused datasets enable the development or refinement of composite drought indices that integrate multiple complementary variables at the field scale. In particular, the combination of high-resolution NDWI, VSDI, TVDI, and LST within a single Agricultural Drought Index allows both vegetation responses and surface moisture conditions to be effectively represented. Together, these advances provide a robust and context-specific framework for agricultural drought monitoring in the Iranshahr-Bampur watershed, a data-scarce semi-arid region where conventional observation networks are limited, with the potential of extending it to other regions after rigorous testing.

2. MATERIALS AND METHODS

2.1. Study area

Iranshahr County is located in the southeastern part of the Iranian Plateau at the center of Sistan and Baluchestan Province (27°12′-27°55′ N, 60°34′-61°15′ E). Covering approximately 17 431 km², it is one of the largest administrative units in the province. The region is predominantly flat, with scattered highlands in the northern and western parts. Iranshahr has a hot arid climate characterized by long, extremely hot summers (with mean temperatures frequently exceeding 35°C), short, mild winters (10-20°C), and very low annual precipitation, typically below 150 mm. Rainfall occurs mainly during sporadic events in the cooler months, while potential evapotranspiration far exceeds precipitation. These conditions strongly influence local vegetation, which is dominated by drought-tolerant and desert-adapted species, and water resources, which rely primarily on groundwater and seasonal rivers (Fig. 1). Agricultural production is limited by water availability and relies primarily on wells, qanats, and seasonal surface flows (*e.g.*, from the Bampur River) for irrigation. Many cultivated fields are in alluvial plains and intermountain valleys with soils ranging from sandy loam to clay loam, and generally low organic matter content. Due to water constraints, single-cropping systems dominate. Wheat is the main staple crop, while rice is grown on smaller, controlled plots during April-September, often using drought-tolerant cultivars. As a result, agricultural productivity in Iranshahr is highly sensitive to climatic variability and water stress, making the region well suited for evaluating advanced drought-monitoring approaches.

2.2. Data

This study uses data from the Terra MODIS and Landsat-8 OLI/TIRS sensors to generate synthetic Landsat-8 imagery with high temporal resolution using the STI-FM model. The fusion was applied to the BLUE, RED, near-infrared (NIR), shortwave infrared (SWIR), and thermal bands following standard atmospheric and radiometric corrections. MODIS and Landsat-8 were selected due to their well-documented compatibility, including similar orbital characteristics, sun-synchronous polar orbits, comparable overpass times (approximately 10:00-10:30 local time), and overlapping spectral bands, particularly in the thermal infrared region in the 10-12 μm range (Feng *et al.*, 2012; Gao *et al.*, 2006; Masek *et al.*, 2006). Archived MODIS and Landsat-8 images were acquired for coincident or near-coincident (the nearest available dates in cases of missing or corrupted imagery) dates during April,

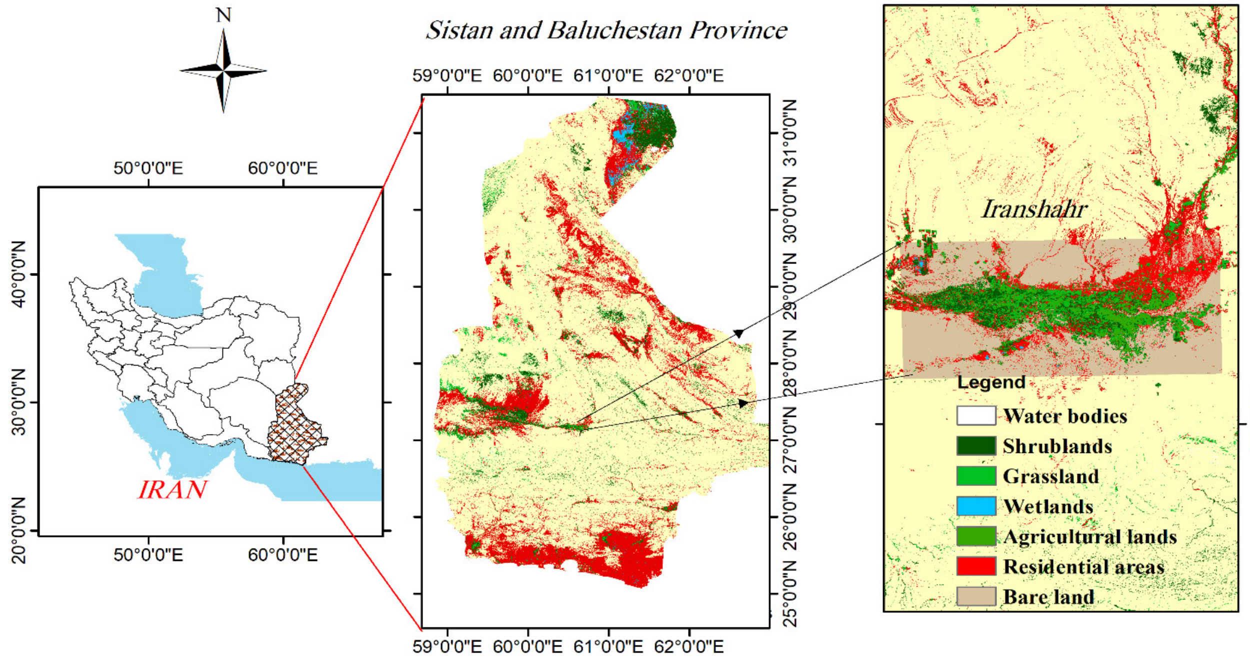

Fig. 1. Geographic setting and land-cover classification for Iranshahr County in Sistan and Baluchestan Province, Iran. The inset maps show land-cover types (water bodies, shrublands, grasslands, wetlands, agricultural lands, residential areas, bare land).

Table 2. Overview of Landsat-8 and MODIS datasets, including acquisition dates, sensor characteristics, and spatiotemporal resolutions, used in the development and evaluation of STI-FM

Acquisition dates		Satellite/Source	Data type	Spatial resolution	Temporal resolution
13 May 29 May	2014	LANDSAT 8	Surface reflectance data, LST	30 m x 30 m 100 m x 100 m	16-day intervals
30 April 16 May	2015				
16 April 2 June	2016				
3 April 19 April	2017				
6 April 22 April	2018				
13 May 14 May 30 May	2014	MODIS	LEVEL 1B calibrated radiances for 7 discrete bands located in the 0.45-2.20 µm region (MOD02HKM), LST (MOD11A1)	500 m x 500 m (MOD02HKM), 1000 m x 1000 m (MOD11A1)	daily
29 April 7 May 16 May	2015				
17 April 25 April 2 June	2016				
4 April 12 April 19 April	2017				
7 April 14 April 23 April	2018				
April 2002 – April 2017		GRACE / TWS	CSR Mascon RL06 mass concentration (mascon) gravity field solutions (NETCDF)	–	–
1987-2018		Iranshahr meteorological station	Precipitation timeseries for the improvement of NDVI prediction for agricultural regions	Localized point	daily

May, and June, which are critical months for crop development and drought assessment in the region. Details of image acquisition dates used for STI-FM implementation and validation are provided in Table 2. Although Landsat 8 became operational in February 2013, suitable images of the study area were unavailable for April-2013 and April 2014; consequently, the first usable image was acquired on 13 May 2014. Landsat 7 imagery was excluded due to the Scan Line Corrector (SLC-off) failure, which causes data gaps and significantly reduces spatial coverage, making it unsuitable for image fusion applications (Landsat, 2014).

The selected spectral bands are widely used for assessing vegetation greenness and surface moisture conditions, particularly during short time intervals in active growing seasons. Based on these bands, several drought-related indices were derived, including the normalized difference vegetation index (NDVI) (Tucker and Choudhury, 1987), the Normalized Difference Water Index (NDWI) (Gao, 1996), the Temperature Vegetation Dryness Index (TVDI), the Visible and Shortwave Infrared Drought Index (VSDI) (Zhang *et al.,* 2013), and Land Surface Temperature (LST). Among these, TVDI was selected as a key indicator due to its high sensitivity to soil moisture and surface dryness in small, semi-arid regions with limited topographic and atmospheric heterogeneity (Kimura, 2007; Rahimzadeh-Bajgiran *et al.*, 2012; Srivastava *et al.*, 2016). Together, these variables form the basis of the ADI. Land cover information was obtained from the MODIS MCD12Q1 annual product, downloaded from the United States Geological Survey portal (https://lpdaacsvc.cr.usgs.gov/appeears/task/area) (Fig. 1). Seven dominant land-cover classes were identified in Sistan and Baluchestan Province: shrublands, wetlands, grasslands, croplands, urban or built-up areas, barren lands, and water bodies. To reduce the computational demands associated with the province's large spatial extent and the 30 m resolution of Landsat imagery, the analysis was limited to a subregion corresponding to a single Landsat scene (Path 157, Row 41) that encompasses the main agricultural areas (Fig. 1).

3. METHODOLOGY

3.1. Spatial-temporal image fusion model (STI-FM)

The STI-FM, developed by Hazaymeh and Hassan (2015), was employed in this study to generate synthetic Landsat-8 imagery by integrating two MODIS images acquired at times t_1 and t_2 [$M(t_1)$, $M(t_2)$] with a Landsat-8 image acquired at t_1 [$L(t_1)$]. The fusion was applied to selected Landsat-8 OLI and TIRS bands, including the BLUE, RED, near-infrared (NIR), shortwave infrared (SWIR), and thermal bands (Table 3). The visible bands (Bands 2 and 4) were used to provide natural color representation and fundamental land cover information, supporting the discrimination of major surface features. The NIR band (Band 5) played a central role in vegetation monitoring, as it is highly sensitive to plant vigor, leaf structure, and biomass levels. This band is critical for assessing vegetation health and detecting subtle changes in crop condition during the growing season. The SWIR band (Band 6) was selected for its strong sensitivity to vegetation and soil moisture, which allowed effective differentiation between wet and dry surfaces. Finally, the TIR band (Band 10) was used to derive Land Surface Temperature (LST), a key variable for characterizing surface energy balance and detecting vegetation water stress. Together, these bands provide complementary information essential for agricultural drought monitoring.

Prior to fusion and index calculation, Landsat-8 reflective and thermal data were preprocessed using standard geometric, radiometric, and atmospheric corrections. Digital numbers (DNs) were converted to surface reflectance and land surface temperature (LST) to ensure consistency and physical interpretability of the input data.

Table 3. Spectral characteristics of the selected operational land imager (OLI) and thermal infrared sensor (TIRS) bands (Landsat, 2014)

Band	
Number	Description
2	BLUE (0.450 - 0.51 μm) 30 m
4	RED (0.64 - 0.67 μm) 30 m
5	Near-Infrared NIR (0.85 - 0.88 μm) 30 m
6	SWIR 1(1.57 - 1.65 μm) 30 m
10	TIRS 1 (10.6 - 11.19 μm) 100 m

a) Conversion of DN values to surface reflectance

Digital number (DN) values were first converted to Top-of-atmosphere (TOA) reflectance using the equation (Landsat, 2014):

$$\rho_{TOA}=\frac{Mult_{ref}*DN-Add_{ref}}{\sin(\theta_{SE})}, \quad (1)$$

where: ρ_{TOA} is the *TOA* reflectance, $Mult_{ref}$ is the band-specific multiplicative scaling factor (REFLECTANCE_MULT_BAND_x in the metadata file, where x is the band number), Add_{ref} is the band-specific additive rescaling factor (REFLECTANCE_ADD_BAND_x in the metadata file), and θ_{SE} is the local sun elevation angle, obtained from the metadata file. The TOA reflectance was subsequently converted to surface reflectance using a simplified atmospheric correction approach that does not require explicit knowledge of atmospheric conditions at the time of image acquisition.

b) Conversion of DN values to land surface temperature

Usually, to convert DN Values from Landsat 8 thermal bands to land surface temperature (LST), DN values are first converted to Top-of-Atmosphere (TOA) spectral radiance (L_λ) using the formula $L_\lambda=MDN+A$, where M is the band-specific multiplicative scaling factor, A is the band-specific additive scaling factor, and DN is the digital number value of each pixel in the image bands. The satellite brightness temperature (T_b) is then calculated as $T_b=\frac{K_2}{ln\frac{K_1}{L_\lambda}+1}$, where T_b is the brightness temperature in Kelvin, and K_1 and K_2 are band-specific thermal conversion constants. The values of M, A, K_1, and K_2 are available in the metadata file accompanying each Landsat 8 image. Finally, the LST is estimated by correcting the brightness temperature for surface emissivity ε, which varies with land cover type. The surface emissivity is typically derived from the normalized difference vegetation index (NDVI), following an NDVI-based emissivity correction method.

In this study, LST was derived directly from the Landsat 8 TIR bands (Band 10) using the radiative transfer method combined with the NDVI-based emissivity correction, following Yu *et al.* (2014). This approach accounts for both atmospheric effects and surface emissivity variations, improving LST accuracy across different land cover types.

c) Regression analysis for Landsat 8 image generation in STI-FM

Within the STI-FM framework, synthetic Landsat 8 imagery $L_{synth}(t_2)$ at time t_2 was generated by establishing a regression relationship between two MODIS images $M(t_1)$ and $M(t_2)$ acquired at times t_1 and t_2. The fusion procedure consists of three main steps:

- Change ratio calculation: For each spectral band, the ratio of change between MODIS images $M(t_1)$ and $M(t_2)$ was calculated to quantify temporal changes in surface reflectance.

- Change-type clustering: The resulting ratio image was classified into three change categories based on the magnitude and direction of reflectance variation, assuming a typical natural variability of approximately ±15% (Ahrens, 2015):
    - $M(t_1) \approx M(t_2)$ – minor change,
    - $M(t_1) > M(t_2)$ – negative change,
    - $M(t_1) < M(t_2)$ – positive change.
- Regression modeling: For each cluster, pixel-wise scatterplots of $M(t_1)$ *vs*. $M(t_2)$ were generated, and linear regression models were fitted to characterize the statistical relationship between the MODIS reflectances at the two time points.

A conceptual illustration of $M(t_1)$ *vs*. $M(t_2)$ scatterplots for three clusters is presented in Fig. 2. The resulting regression relationships were subsequently used to predict the finer-resolution Landsat 8 image at time t_2 following the STI-FM framework (Hazaymeh and Hassan, 2015). For the land surface temperature (LST) band, a single pixel-wise regression relationship between $M(t_1)$ and $M(t_2)$ was applied without change-based clustering. This approach follows methodologies widely adopted in previous studies (Hazaymeh and Hassan, 2015; Meng *et al.*, 2025b; Yu *et al.*, 2023), which have shown that a single regression model sufficiently captures the temporal dynamics of LST in coarse-to-fine data fusion.

d) Generating synthetic Landsat 8 imagery *via* regression coefficients and upscaling

Once the regression relationships between $M(t_1)$ and $M(t_2)$ are established, the derived coefficients (slope and intercept) are applied to the Landsat 8 image $L(t_1)$. This step produced synthetic Landsat 8 images at 30 m spatial resolution for time t_2, combining the spatial detail of Landsat with the temporal dynamics captured by MODIS (Hazaymeh and Hassan, 2015). The resulting synthetic surface reflectance and LST maps thus provide enhanced spatiotemporal coverage for drought analysis.

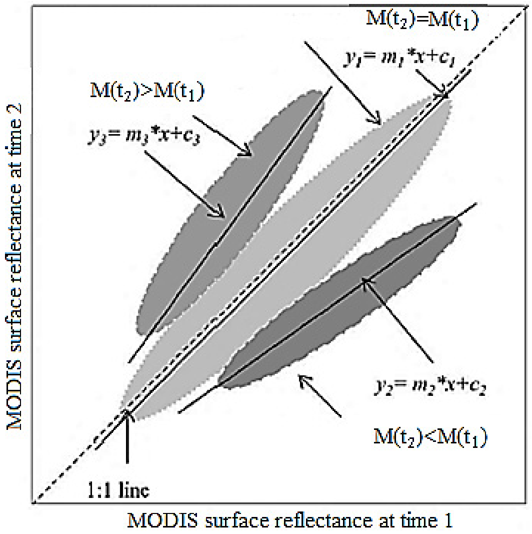

Fig. 2. Conceptual representation of the pixel-wise relationship between two MODIS images acquired at different times ($M(t_1)$ and M(t2)). The scatter of points is divided into three clusters-minor, negative, and positive change-based on the ratio of temporal reflectance differences.

The STI-FM method relies on two key assumptions. First, it assumes a linear relationship between consecutive MODIS observations, which is reasonable for surface reflectance and LST when land cover remains stable (Hassan *et al.,* 2007). Second, it assumes comparability between Landsat 8 and MODIS observations acquired at the same time, as both sensors operate under similar viewing geometries and atmospheric conditions (Gao *et al.,* 2006). Based on these assumptions, once the regression relationships between $M(t_1)$ and $M(t_2)$ are established, the derived coefficients (slope and intercept) can be applied to the Landsat 8 image $L(t_1)$ at time t_1 to generate a synthetic Landsat 8 image $L_{synth}(t_2)$ for time t_2.

Model performance was evaluated using a cross-validation strategy. One Landsat 8 acquisition date was intentionally excluded from the fusion process, and a synthetic image was generated for that date using the surrounding MODIS images and the remaining Landsat data. The synthetic image was then compared with the actual Landsat 8 image acquired on the same date, allowing a rigorous assessment of the model's ability to reconstruct Landsat-like imagery for periods without direct observations.

3.1.1. Normalized difference vegetation index (NDVI)

The normalized difference vegetation index (NDVI) is one of the most widely used indicators for assessing vegetation greenness and density, derived from near-infrared (NIR) and red (RED) reflectance (Rouse *et al.*, 1974; Didan *et al.*, 2015):

$$\mathrm{NDVI} = \frac{R_{NIR} - R_{RED}}{R_{NIR} + R_{RED}}. \tag{2}$$

NDVI values for vegetated surfaces typically range from 0.5 to 1.0, with higher values indicating denser and healthier vegetation. Values between 0.1-0.5 refer to rather sparse vegetation or areas with low-density plant cover. Values below 0.1 generally correspond to bare soil, while negative values are associated with water, snow, or ice. The MODIS Vegetation Index product (MOD13A3), a monthly composite, was used in this study. These products are atmospherically and radiometrically corrected and are therefore suitable for direct analysis. All MODIS data were obtained from the NASA Earthdata Search portal (https://search.earthdata.nasa.gov).

3.1.2. Normalized difference water index (NDWI)

The Normalized Difference Water Index (NDWI) uses the near-infrared (NIR) and shortwave infrared (SWIR) spectral bands reflectance to assess vegetation water content and monitor drought conditions (Fensholt and

Sandholt, 2003; Gao, 1996; Wang and Qu, 2009). In this index, the NIR band provides a reference for vegetation biomass reflecting the structure of plant leaves, while the SWIR band is highly sensitive to changes in vegetation moisture (Zhang *et al.*, 2013):

$$\mathrm{NDWI} = \frac{\mathrm{R_{NIR}} - \mathrm{R_{SWIR}}}{\mathrm{R_{NIR}} + \mathrm{R_{SWIR}}}. \tag{3}$$

NDWI values range from –1 to +1, with higher positive values indicating greater vegetation water content (healthy, well-watered crops). Values near zero reflect moderate moisture conditions, while negative values indicate water stress or drought, with limited water present in the vegetation.

3.1.3. Visible and shortwave infrared drought index (VSDI)

The visible and shortwave infrared drought index (VSDI) was developed for agricultural drought monitoring and tested over Oklahoma (Zhang *et al.*, 2013). It employs the SWIR, RED, and BLUE bands. The index exploits the strong sensitivity of SWIR and RED reflectance to soil and vegetation moisture, while the BLUE band serves as a reference due to its lower sensitivity:

$$VSDI = 1 - ((\mathrm{R_{SWIR}} - \mathrm{R_{BLUE}}) + (\mathrm{R_{RED}} - \mathrm{R_{BLUE}})). \tag{4}$$

VSDI values are positive, with values between 0 and 1 indicating increasing soil and vegetation wetness as the index approaches 1. Values exceeding 1 are typically associated with water bodies, snow, or ice.

3.1.4. Temperature and vegetation dryness index (TVDI)

Sandholt *et al*. (2002) identified characteristic contours in the feature space defined by the normalized difference vegetation index (NDVI) and land surface temperature (LST), based on which the TVDI was developed. It is defined as (Gao *et al.*, 2011; Sandholt *et al.*, 2002):

$$\mathrm{TDVI} = \frac{\mathrm{LST} - \mathrm{LST_{min}}}{\mathrm{LST_{max}} - \mathrm{LST_{min}}}, \tag{5}$$

where: $\mathrm{LST_{min}} = a_1 + b_1 \times \mathrm{NVDI}$, and $\mathrm{LST_{max}} = a_2 + b_2 \times \mathrm{NVDI}$. LST is the land surface temperature corresponding to each pixel. $\mathrm{LST_{min}}$ and $\mathrm{LST_{max}}$ represent the minimum and maximum *LST* values, respectively, for each NDVI value, defining the so-called wet and dry edges. The coefficients a_1, b_1 and a_2, b_2 are the regression parameters for these edges. TVDI values range from 0 to 1, where lower values indicate wetter (more humid) conditions and higher values indicate drier conditions.

3.1.5. MODIS land surface temperature (LST)

MODIS land surface temperature (LST) was obtained from MODIS Level-3 products, which are generated by temporal aggregation of Level-2 observations and are provided with atmospheric and radiometric corrections applied. In this study, MODIS LST data (specifically MOD11A1) were acquired from the NASA Earthdata Search Portal (https://search.earthdata.nasa.gov).

3.1.6. Agricultural drought index (ADI)

The ADI was constructed by integrating four drought-sensitive variables: NDWI, VSDI, TVDI, and LST, calculated at 8-day intervals. To minimize redundancy, indices with low inter-correlation were selected. For each variable, mean values over the study period were used as reference thresholds to distinguish dry and wet conditions. Pixels with NDWI and VSDI values below their respective means were classified as dry, while pixels with LST and TVDI values above their means were considered dry. Drought maps were first generated for each variable and then combined to produce the ADI. Based on the number of variables indicating dry conditions, pixels were classified into five drought severity categories: extreme (four variables), severe (three), moderate (two), mild (one), and wet (none). ADI maps were generated using both actual and synthetic Landsat 8 imagery.

3.1.7. Standardized precipitation index (SPI)

The SPI was used to validate the ADI maps generated at 8-day intervals. SPI is a widely applied meteorological drought indicator based solely on precipitation data, with negative values indicating dry conditions and positive values indicating wet conditions. One of the key advantages of SPI is its flexibility: it can be calculated over various accumulation periods (*e.g.*, 1, 3, 6, 12, or 24 months), allowing the assessment of drought impacts ranging from short-term soil moisture deficits to long-term hydrological shortages (Poudel *et al.,* 2024). Despite its usefulness, the primary limitation of SPI lies in its exclusive reliance on precipitation. It does not account for other climatic factors such as temperature, evapotranspiration, or changes in land surface conditions, which may intensify drought impacts, particularly under warming climate scenarios (Lorenzo-Lacruz *et al.*, 2010).

In this study, SPI was calculated using 30 years (1989-2018) of daily precipitation data from the Iranshahr meteorological station. A 5-year subset (2014-2018) corresponding to the study period was used for direct comparison with the ADI, while the full record provided the long-term drought context.

3.1.8. Hydrological drought deficit and severity indices

Hydrological drought conditions were assessed using satellite-based data from the gravity recovery and climate experiment (GRACE) for the period 2002-2018. GRACE detects temporal variations in Earth’s gravity field, which can be converted into changes in terrestrial water storage (TWS). Unlike precipitation-based indices, GRACE-derived TWS integrates multiple hydrological components, including groundwater, soil moisture, surface water, snow, and ice (Lenczuk *et al.,* 2024). The capability of capturing subsurface water changes, particularly groundwater depletion, is especially valuable in arid and semi-arid regions, where groundwater plays a critical role and *in-situ* observations are often limited (Ren *et al.,* 2026). Consequently, GRACE-based drought indices provide a more comprehensive assessment of drought severity and persistence and are well suited for large, data-scarce regions such as eastern Iran.

This study follows the approach of Thomas *et al.* (2014), with a slight modification in the calculation of drought deficit. Instead of computing the deficit as the negative deviation of monthly terrestrial water storage anomalies (TWSA) from the long-term mean, deficit months were defined as those with negative TWSA values only (Almamalachy *et al.*, 2020). To capture the combined effect of drought deficit magnitude and its persistence, drought severity was introduced. For month *i*, severity is calculated as the mean deficit from the onset of drought up to the current month, multiplied by the duration (in months) of the drought event. Equivalently, severity can be expressed as the cumulative deficit over the drought period (Thomas *et al.*, 2014; Madadgar and Moradkhani, 2014):

$$Severity_{(n)} = \sum_{1}^{i=n} Deficit_{(i)}, \tag{6}$$

where: *n* denotes the number of months since drought onset. Severity is expressed in km^3 × month, and the total severity of a drought event is obtained at the last month before drought termination.

4. RESULTS

4.1. Synthetic Landsat-8 images from the STI-FM fusion model

Synthetic Landsat-8 imagery was generated using the STI-FM fusion model by establishing pixel-wise relationships between MODIS images acquired at two times, M(t_1) and M(t_2). This procedure was applied to all MODIS observations collected during the growing seasons (April–June) from 2014 to 2018 for the BLUE, RED, NIR, SWIR, and LST bands. Figure 3 illustrates representative scatterplots for MODIS image pairs acquired on 17 and 25 April 2016, while additional examples are provided in Figs S1-S4 (Supplementary Material SM1). In the scatterplots for the reflective bands, points are color-coded with three distinct colors to represent different change ratios (blue = positive change, red = minor change, black = negative change), while for the LST band, a single pixel-wise regression relationship between MODIS images at M(t_1) and M(t_2) was applied without any clustering by change type. Strong linear relationships were observed across all spectral and thermal bands, characterized by high coefficients of determination (R^2), consistent regression parameters, and stable value ranges. These results confirm the robustness of the MODIS-based relationships used to generate synthetic Landsat-8 imagery.

The derived regression coefficients were subsequently applied pixel-wise to Landsat images at L(t_1) to generate synthetic Landsat 8 images at $L_{synth}(t_2)$. Model accuracy was evaluated through cross-validation by generating a synthetic image for a date with an available Landsat acquisition and comparing it directly with the observed data. Figure 4 presents pixel-wise comparisons for the BLUE, RED, NIR, SWIR, and LST bands on 30 May 2014, with additional dates shown in Figs S5-S8 (Supplementary Material SM1). The synthetic and observed images show good agreement between observed and synthetic data, reflected by very high R^2 values and low error metrics (Root Mean Squared Error RMSE and Absolute Average Deviation AAD), indicating that the STI-FM model reliably reproduces both spectral and thermal characteristics at Landsat resolution.

Qualitative validation is shown in Fig. 5, which compares observed and synthetic maps of NDWI, TVDI, VSDI, and LST for 30 May 2014, along with their corresponding histograms. The spatial patterns and value distributions are highly consistent across all indices, particularly over agricultural areas. Minor discrepancies, such as slightly elevated LST or reduced NDWI and TVDI values, are mainly confined to barren and non-agricultural surfaces. Importantly, the synthetic LST images successfully capture dominant land cover types, such as vegetation and cultivated fields, with high accuracy. Overall, these findings confirm that the fusion approach accurately preserves both thermal and spectral-biophysical characteristics of the land surface.

4.2. STI-FM fusion-based agricultural drought index (ADI)

High temporal and spatial resolution synthetic Landsat 8 imagery generated with the STI-FM fusion model were used to monitor drought conditions in the Iranshahr region during the growing seasons from 2014 to 2018. The ADI was constructed by integrating four uncorrelated variables-NDWI, VSDI, TVDI, and LST-derived from both actual and synthetic Landsat 8 imagery. Although ADI maps were produced for all acquisition dates, three representative periods (13 May 2014, 30 April 2015, and 22 April 2018) were selected for the discussion (Fig. 6), whereas ADI maps for the remaining dates are shown in Fig. S9 (Supplementary Material SM1). These examples illustrate pronounced spatial and temporal variability in drought severity across the region and provide a clear visualization of agricultural conditions during the analyzed periods. The ADI maps, supplemented with pie charts, depict the proportional distribution of drought severity classes, with no occurrence of a non-drought class during the study period,

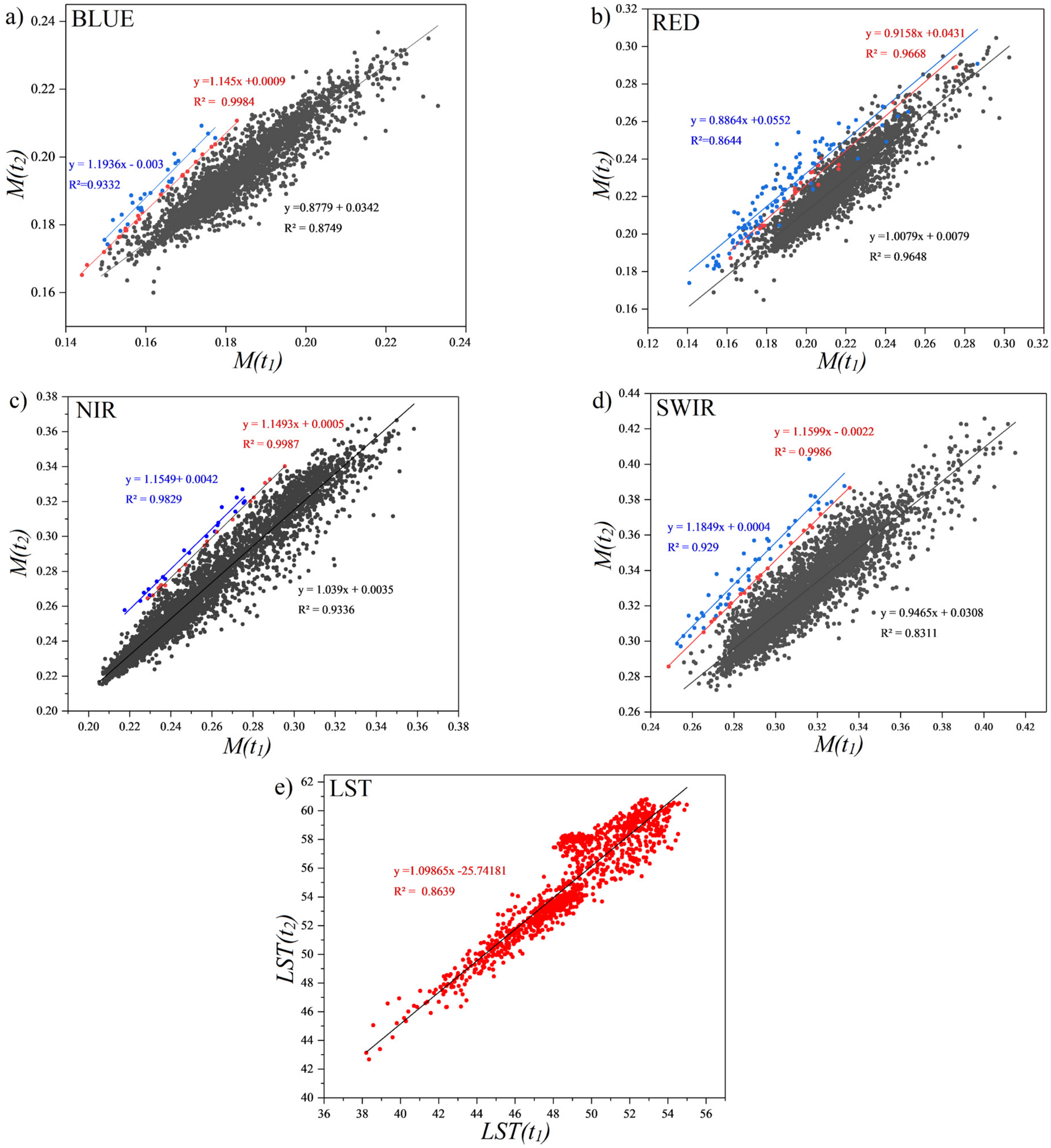

Fig. 3. Pixel-wise scatterplots illustrating the relationships between MODIS reflectances acquired on 17 April 2016 (M(t_1)) and 25 April 2016 (M(t_2)) for bands: a) BLUE, b) RED, c) NIR, d) SWIR), and e) LST. Points are clustered according to change ratios, where blue color indicates positive changes, red represents minor changes, and black corresponds to negative changes.

highlighting ongoing water stress over agricultural lands. Several agricultural zones exhibit particularly high drought severity, reflecting sustained water stress.

4.3. Meteorological and hydrological validation of ADI

The ADI was validated through a two-stage approach combining meteorological and hydrological analyses, following established drought-assessment frameworks (Famiglietti *et al.*, 2011; Vicente-Serrano *et al.*, 2010). Meteorological validation was performed by comparing ADI with the standardized precipitation index (SPI) for the Iranshahr region. SPI was calculated for a 30-year reference period (1989-2018), with values for 2014-2018 extracted to match the ADI analysis period (Fig. 7). The Pearson correlation coefficient between ADI and SPI was –0.334, indicating a weak but consistent negative relationship, with lower SPI values (representing more severe meteorological drought) corresponding to higher ADI values.

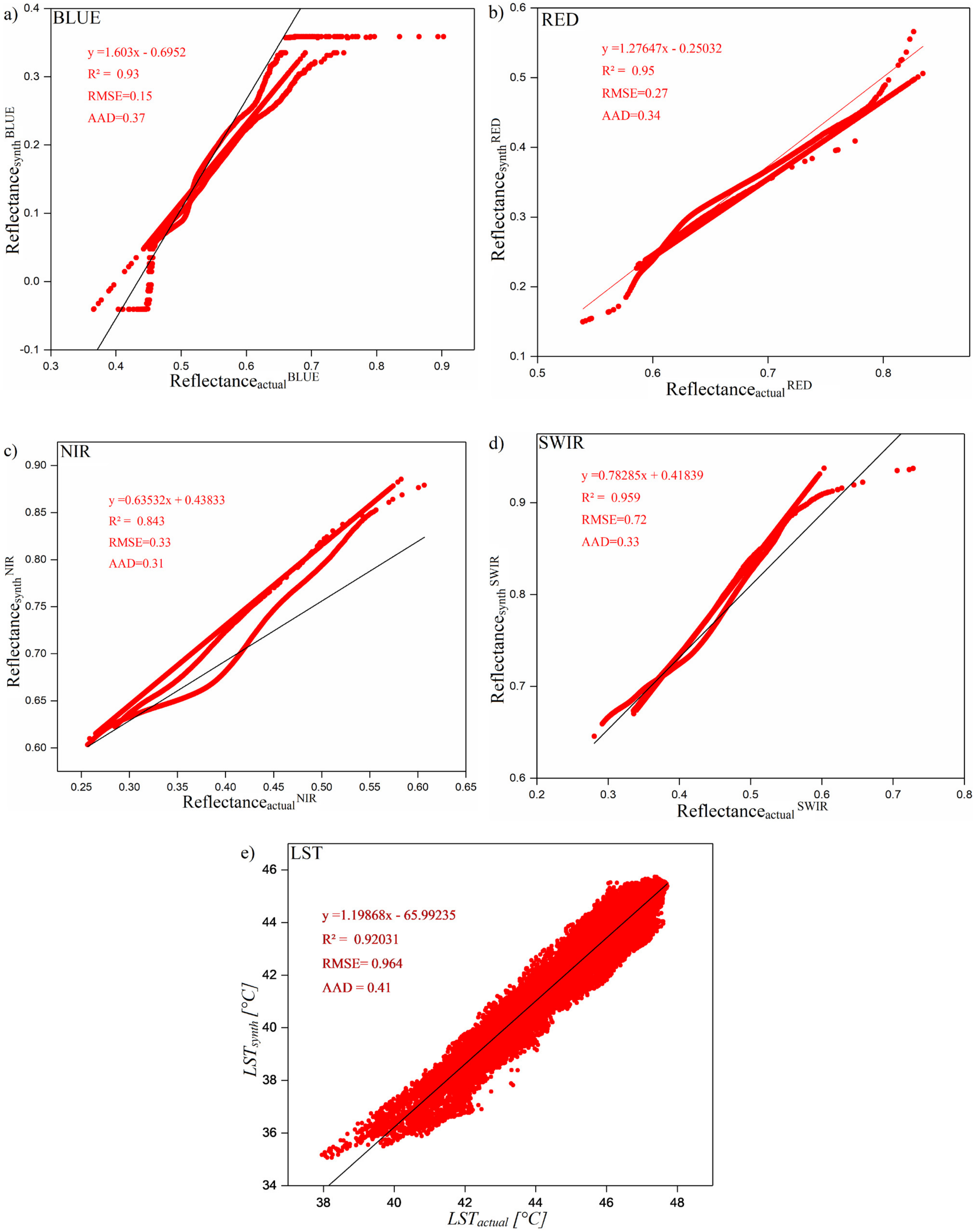

Fig. 4. Scatterplots comparing the actual and synthetic values from the four Landsat 8 reflective bands: a) BLUE, b) RED, c) NIR, d) SWIR and e) LST for 30 May 2014.

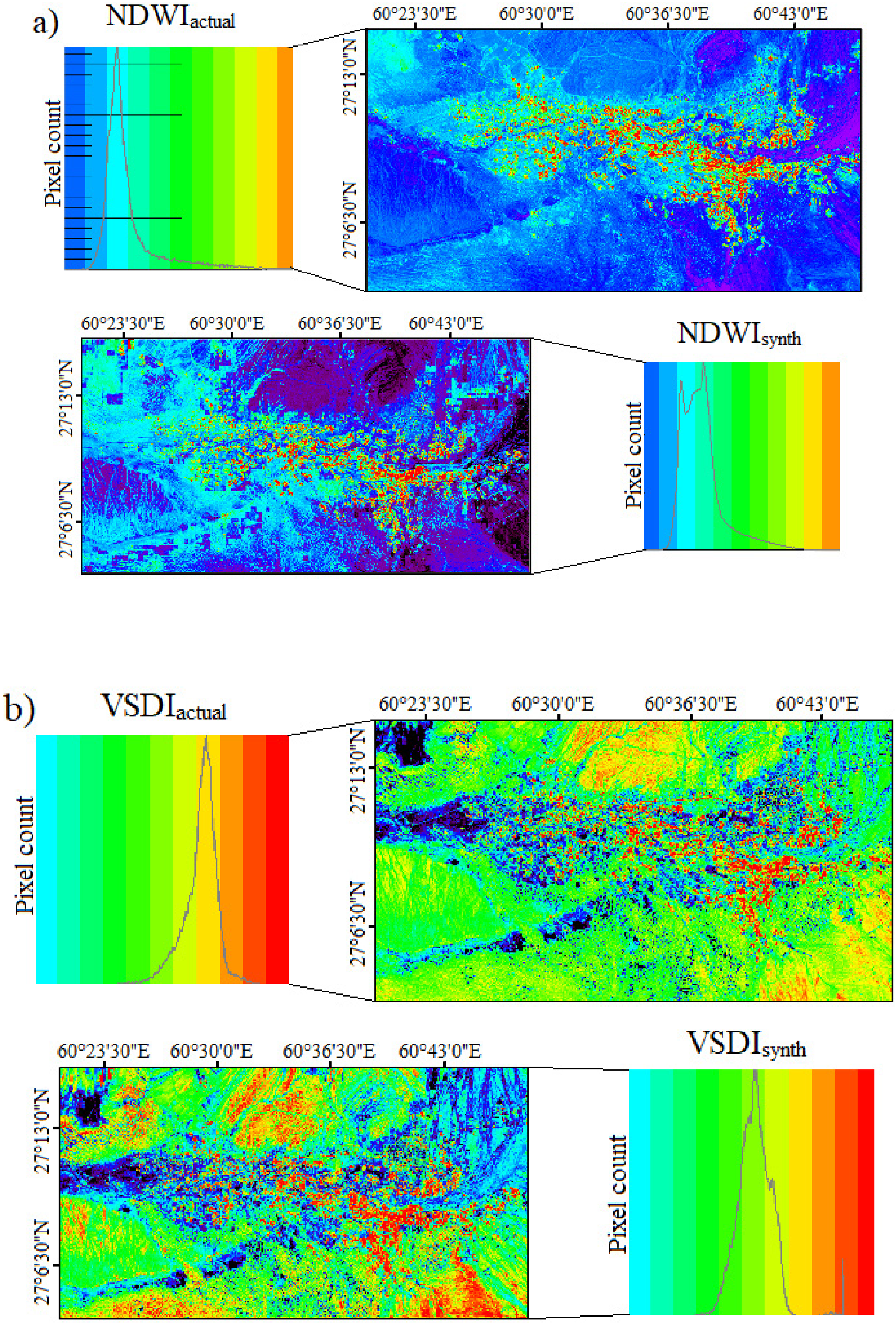

Fig. 5. Comparison of actual and synthetic Landsat 8-derived maps of: a) the normalized difference water index (NDWI), b) the vegetation soil dryness index (VSDI), c) the temperature-vegetation dryness index (TVDI), and d) the land surface temperature (LST) for 30 May 2014 over the assessed agricultural subregion of the Iranshahr area. For each index, the upper panel shows the actual image and the lower panel shows the synthetic image, while adjacent insets present the associated histograms (pixel count versus index value). Histogram colors correspond to those used in the map visualizations.

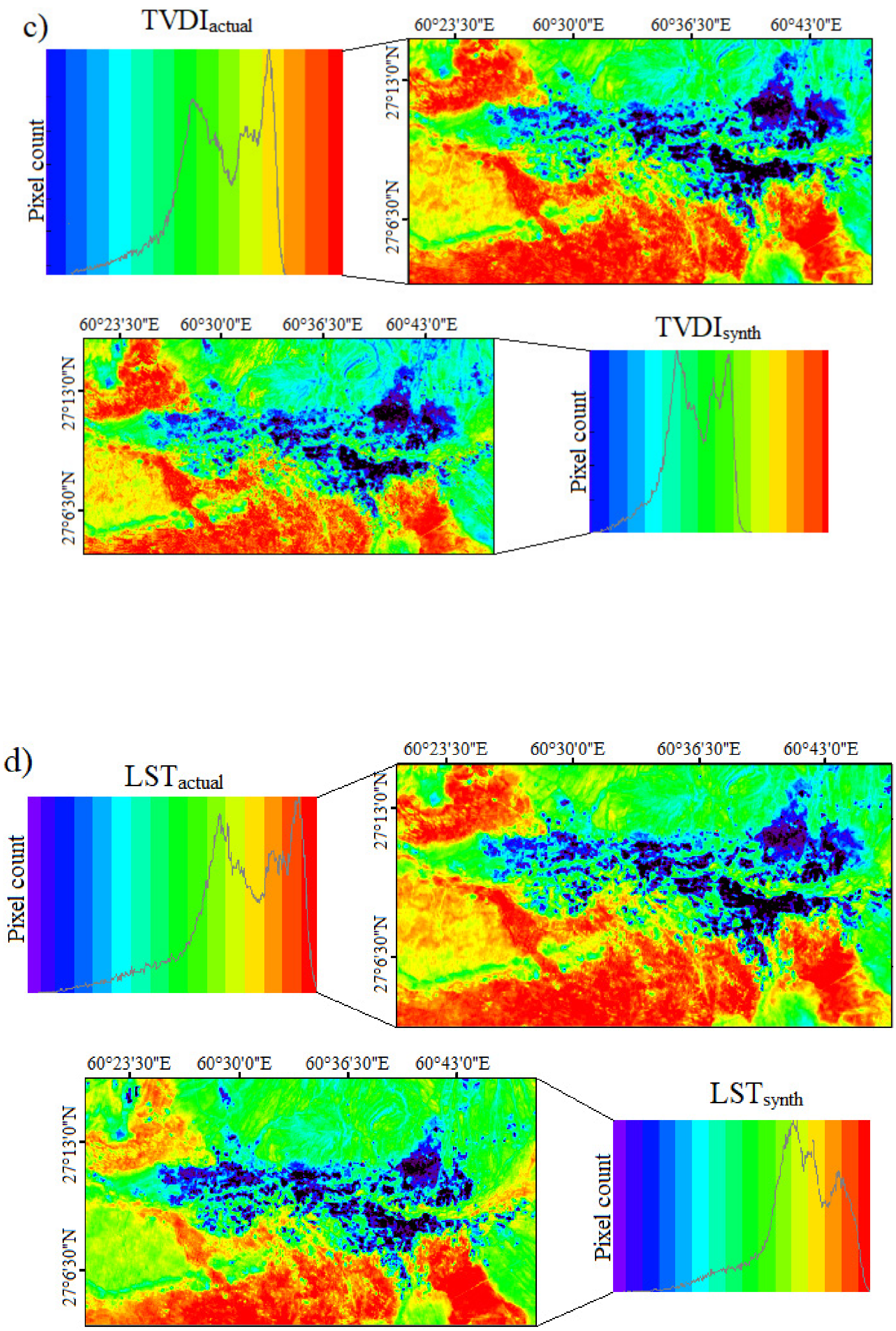

Fig. 5. Continuation.

a) 13 May 2014

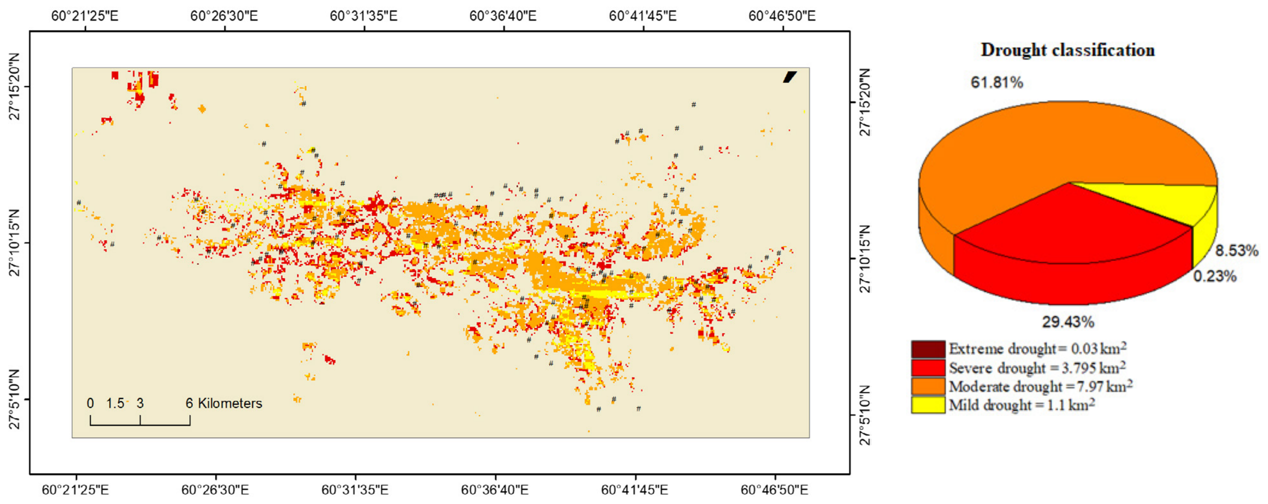

b) 30 Apr 2015

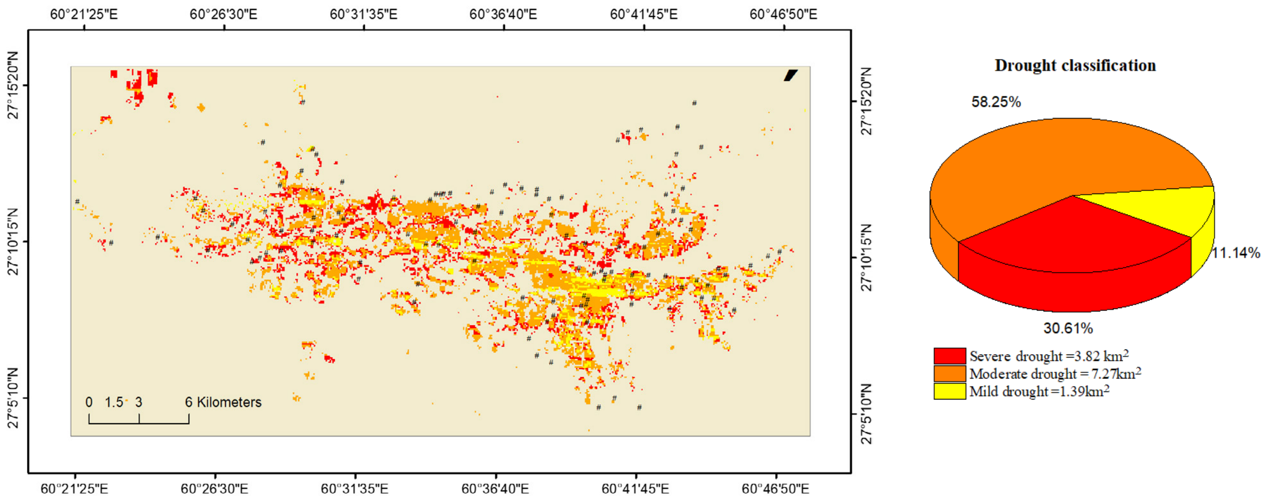

c) 22 Apr 2018

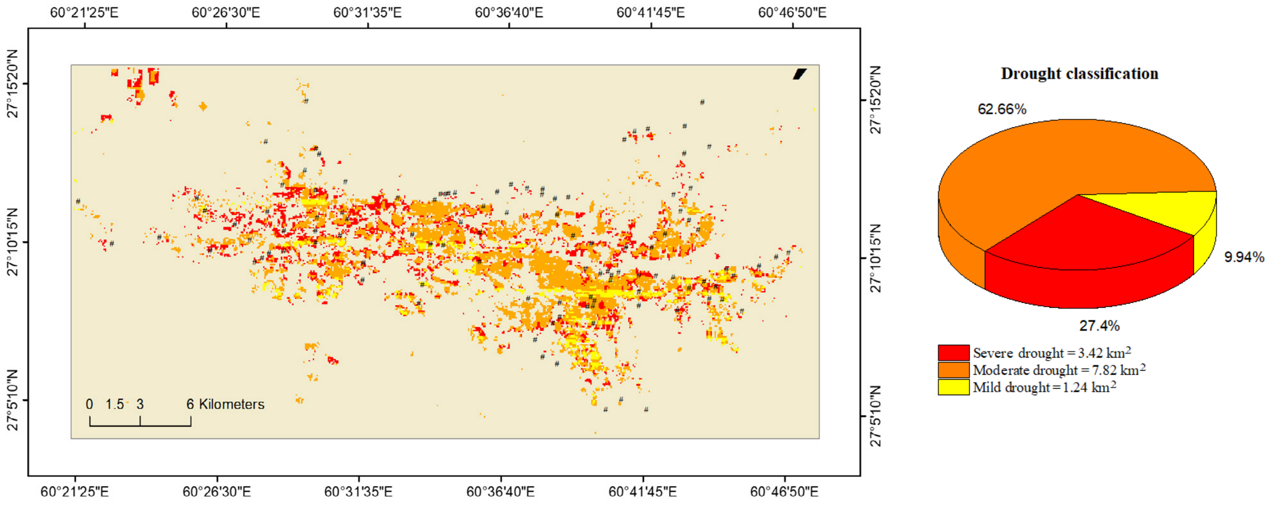

Fig. 6. Agricultural drought index (ADI) maps (left) and corresponding pie charts illustrating the proportional extent of drought severity classes (right) for the assessed agricultural subregion of the Iranshahr area for: a) 13 May 2014, b) 30 April 2015, and c) 22 April 2018.

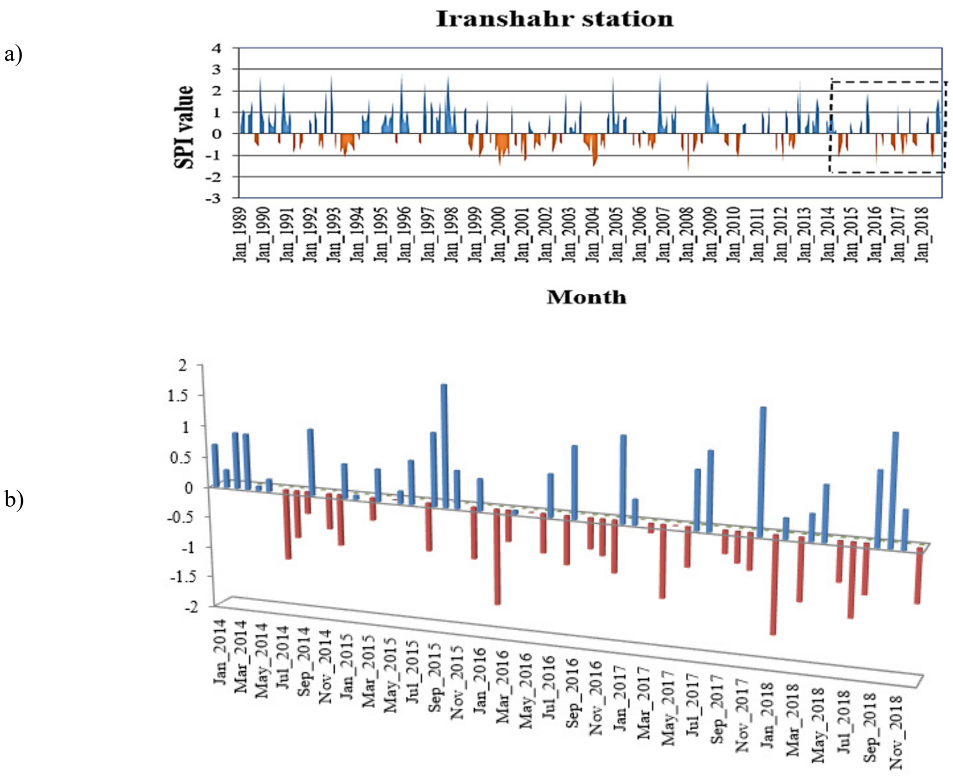

Fig. 7. Temporal variations of the standardized precipitation index (SPI) over the Iranshahr region for the periods: a) 1989-2018 and b) 2014-2018.

Table 4. Hydrological drought characteristics of the Iranshahr-Bampour watershed in southeastern Iran obtained from GRACE/GRACE-FO terrestrial water storage anomalies

Basin name	Area (km^2)	Number of drought periods > 4 months	Duration of each period	Coincidence with meteorological drought	Period (months)	Average deficits	Total severity
Iranshahr-Bampour	10 053.98	6	March 2011-June 2017	yes	76	-5.86	-445.06

Hydrological validation was performed using GRACE/GRACE-FO terrestrial water storage anomalies (TWSA) for the Iranshahr-Bampur watershed. Negative TWSA values indicate below-average water storage and hydrological drought. Based on the criteria of Long *et al.* (2015), six drought events lasting longer than four months were identified (Table 4). The most prolonged event extended from March 2011 to June 2017 (76 months), with an average monthly deficit of 5.86 km³ and a cumulative severity of 445.06 km³ x month. Isohyet maps (Fig. 8) show mean annual precipitation of only 100-110 mm, confirming the basin's extreme aridity. Recovery estimates indicate that approximately 30 consecutive months of above-normal precipitation would have been required to restore normal hydrological conditions by mid-2016, highlighting the persistence of the deficit. Due to the fundamental differences in spatial resolution and dataset characteristics, no direct statistical correlation between ADI (~30 m resolution) and GRACE TWSA (~300 km resolution) was performed. Instead, GRACE TWSA were used qualitatively to characterize basin-scale hydrological drought, providing complementary context alongside ADI-based meteorological and agricultural assessments. Despite this scale mismatch, the temporal correspondence between sustained negative GRACE anomalies and elevated ADI values is observed, which demonstrates that the ADI effectively captures not only short-term agricultural drought but also longer-term hydrological stress.

Together, the results shown in Fig. 7, Table 4, and Fig. 8 confirm that the proposed ADI is a reliable and physically consistent indicator for agricultural drought monitoring in the Iranshahr-Bampur watershed.

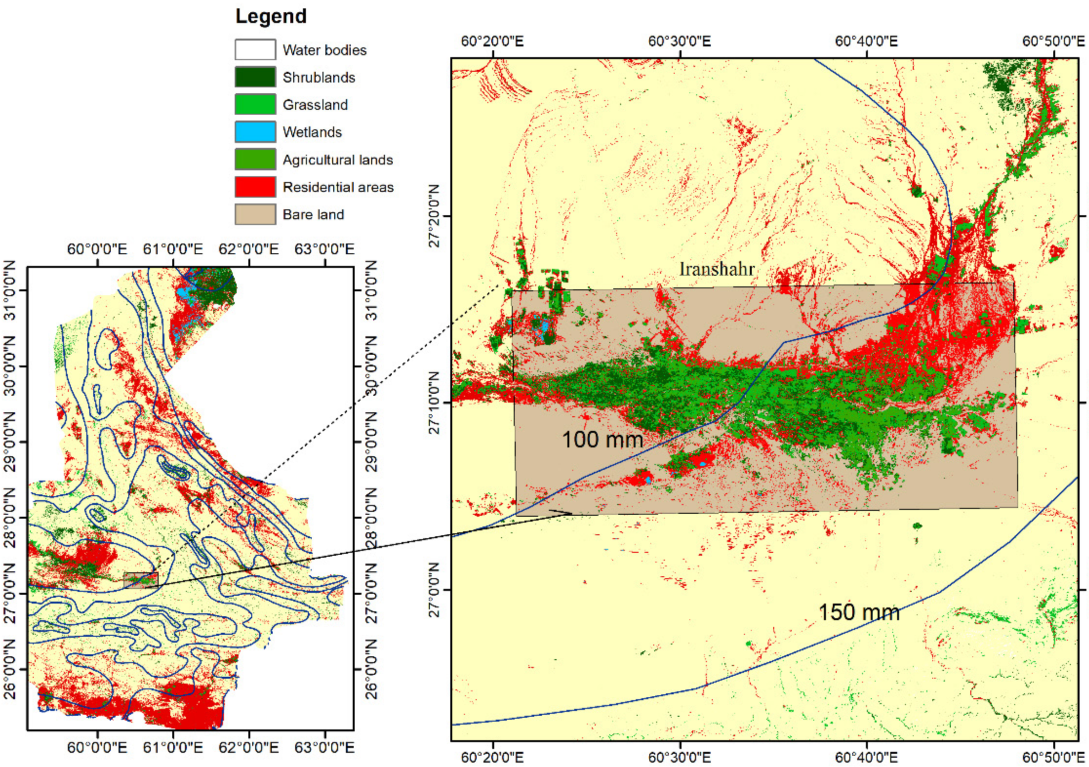

Fig. 8. Map of the Iranshahr study area in Sistan and Baluchestan Province, southeastern Iran, showing watershed boundaries and mean annual precipitation isohyets, illustrating the spatial distribution of rainfall across the region.

5. DISCUSSION

This study demonstrates the effectiveness of a spatiotemporal data fusion framework combining Landsat 8 and MODIS imagery for agricultural drought monitoring in the semi-arid Iranshahr-Bampur region. The STI-FM approach generated high-quality synthetic Landsat 8 reflectance and land surface temperature (LST) data, supported by strong statistical performance ($R^2 > 0.9$, low RMSE and AAD) and close agreement with actual observations. These results are consistent with previous studies showing that data fusion can successfully overcome the spatial-temporal trade-off inherent in satellite observations (Gao *et al.*, 2006; Roy *et al.*, 2015; Zhu *et al.*, 2010). Notably, the performance of the proposed model is comparable to or exceeds that reported in earlier LST fusion studies. For instance, Huang *et al.* (2013) and Liu and Weng (2012) reported correlation coefficients between observed and predicted LST values ranging from 0.72 to 0.83, with RMSE values between 0.96 and 2.6 and AAD values between 0.6 and 2.3 for comparisons between actual and predicted data.

The accuracy of the synthetic Landsat imagery directly influences the reliability of the derived drought indices and, consequently, the ADI classification. The results indicate that the STI-FM fusion model preserves the spectral and thermal signals essential for drought assessment. Because the ADI is based on threshold-based classifications of NDWI, VSDI, TVDI, and LST relative to scene-specific means, moderate reconstruction errors are unlikely to systematically bias drought severity patterns, particularly over homogeneous agricultural areas where the strongest agreement was observed. However, small deviations in synthetic reflectance or temperature values may propagate into index calculations near classification thresholds, potentially affecting drought category assignment at the pixel level, especially in heterogeneous or non-agricultural surfaces. Despite this, the strong spatial and statistical consistency between observed and synthetic indices suggests that fusion-induced uncertainties have a limited impact on the overall spatiotemporal drought patterns captured by the ADI, supporting the robustness of the drought assessment at the field to regional scale.

The ADI, developed by integrating independent drought indicators (NDWI, VSDI, TVDI, and LST), proved effective for capturing drought dynamics in this semi-arid environment. A key strength of the ADI is its use of a dynamic thresholding approach, in which the mean value of each indicator is calculated for the study area at 8-day intervals. As a result, thresholds are scene-specific rather than fixed or arbitrarily defined. This adaptive strategy aligns with established remote sensing practices for drought anomaly detection and enhances sensitivity to local and temporal variability, particularly in heterogeneous semi-arid landscapes (Carlson *et al.*, 1994; Sandholt *et al.*, 2002). By evaluating each indicator relative to its scene-specific mean, the ADI avoids the limitations of global thresholds and ensures that drought classifications reflect prevailing biophysical conditions. Overall, the use of adaptive, data-driven thresholds provides a robust basis for integrating multiple indicators within the ADI framework and strengthens its reliability for agricultural drought monitoring. The ADI consistently identified persistent drought conditions between 2014 and 2018, in agreement with hydrological evidence indicating a prolonged (76-month) drought in the Iranshahr-Bampur watershed. The extremely low mean annual precipitation (~109 mm) estimated *via* isohyetal mapping further emphasizes the region's vulnerability to long-term drought stress, consistent with broader analyses of drought vulnerability in hyper-arid to semi-arid climates (Trambauer *et al.*, 2014). This convergence of meteorological, agricultural, and hydrological indicators aligns with previous research emphasizing the importance of multi-index approaches for robust drought assessment in regions with highly variable precipitation (McVicar *et al.*, 2012; Vicente-Serrano *et al.*, 2004; Zarch *et al.*, 2015). Minor discrepancies between synthetic and observed LST were observed in barren and non-agricultural areas, reflecting known limitations of fusion techniques in heterogeneous landscapes (Roy *et al.*, 2015; Zhu *et al.*, 2010). However, these differences were minimal over cultivated areas and did not affect agricultural drought assessments.

The weak correlation between the ADI and the Standardized Precipitation Index (SPI) (−0.334) is expected in semi-arid agricultural systems, as the two indices capture different aspects of drought. The SPI reflects only precipitation deficits and does not account for surface energy balance or human activities related to irrigation. In contrast, the ADI integrates multiple indicators, including soil moisture conditions (TVDI), vegetation stress (VSDI), and plant water status (NDWI). Moreover, vegetation responses to drought are often delayed, and irrigation practices further decouple soil moisture and crop condition from rainfall variability. In irrigated systems, water availability is therefore not directly linked to precipitation alone. As a result, SPI by itself cannot fully represent agricultural drought conditions. The multi-variable structure of the ADI provides a more accurate and field-scale-relevant assessment of drought impacts on agriculture. Despite the limited number of data points, the weak (negative) relationship between SPI and ADI values is consistent with previous studies reporting modest relationships between precipitation-based and remote sensing–based drought indicators. Comparable correlation ranges have been documented across diverse agro-climatic regions (Liu *et al.*, 2020; Viet and Thuy, 2024; Yao *et al.*, 2025). For example, Yao *et al.* (2025) reported correlations ranging from 0.3 to 0.6 between meteorological drought indices and satellite-derived indicators (*e.g.*, VCI, TCI, VHI, TVDI) across nine agricultural regions of China. Similarly, Liu *et al.* (2020) found correlations between 0.2 and 0.7 between SPEI and remote sensing-based indices (including TCI and VCI) in Shandong Province, located on China's east coast. In a study by Viet and Thuy (2024), weak correlations were observed between SPI and VCI and between SPEI and VCI (0.0-0.2), as well as between SPI and TDVI and SPEI and TDVI (0.0 to −0.2), while moderate correlations were reported for SPI-TCI, SPEI-TCI, SPI-VHI, and SPEI-VHI (0.25-0.55). The results of the present study therefore fall within these reported ranges, supporting the ability of remotely sensed indices to capture key aspects of drought dynamics. Moreover, the moderate correlation aligns with earlier findings showing that vegetation- and soil-based drought indices often exhibit delayed or smoothed responses relative to precipitation-based indicators (Hao *et al.*, 2018; McKee *et al.*, 1993). Regional differences in climate, land use, and vegetation structure further modulate these relationships.

Several limitations should be acknowledged, particularly with respect to the transferability of the proposed ADI framework. Although the index was developed and validated for a semi-arid agricultural system dominated by irrigated and rainfed croplands, its performance may vary in other semi-arid regions characterized by different land-cover compositions, cropping calendars, irrigation intensities, or management practices. The relative sensitivity of the ADI components-especially NDWI and TVDI-may differ in regions with sparse vegetation, perennial crops, or mixed natural-agricultural landscapes, potentially affecting drought classification. The classification of drought conditions relies on threshold values derived from long-term mean conditions of individual variables and, although this approach ensures internal consistency, the threshold selection introduces uncertainty and may influence drought severity classification, especially under non-stationary climatic conditions. Also, all ADI components were treated with equal importance, and no explicit weighting scheme was applied. While this design choice avoids subjective bias, it does not account for potential differences in variable sensitivity across crop types, phenological stages, or management practices. In addition, the STI-FM fusion approach relies on the availability of temporally consistent, cloud-free Landsat and MODIS observations; prolonged cloud cover or strong surface heterogeneity may introduce uncertainties through spatial resampling and regression-based fusion, particularly in non-agricultural or transitional areas. Validation was further constrained by the limited availability of *in-situ* soil moisture, irrigation, and yield data. Consequently, validation relied primarily on established meteorological and hydrological indicators, which were used to provide qualitative and contextual support rather than direct quantitative calibration or pixel-level validation. While this approach is consistent with common practice in data-scarce semi-arid regions, it limits the ability to fully assess the index performance at finer spatial scales.

Overall, the key contribution of this study lies in integrating high-resolution spatiotemporal image fusion with a multi-variable drought index to improve agricultural drought monitoring under the specific environmental and agro-hydrological conditions of southeastern Iran, with potential applicability to other data-scarce semi-arid regions. Although the approach depends on robust regression relationships and is limited by the availability of high-resolution hydrological validation data for comprehensive validation across larger areas, the results demonstrate that the combined STI-FM and ADI framework can characterize agricultural drought dynamics in the semi-arid agroecosystem.

6. CONCLUSIONS

This study successfully implemented and validated a robust spatio-temporal data fusion framework integrating Landsat 8 and MODIS imagery, significantly enhancing agricultural drought monitoring framework in the semi-arid Iranshahr region of southeastern Iran. The methodology, based on linear regression relationships applied to spatially resampled Landsat 8 data, effectively generated high-temporal-resolution synthetic Landsat images across key spectral bands.

A novel remote sensing-based ADI was developed by integrating uncorrelated drought-related variables, including NDWI, VSDI, TVDI, and LST. The incorporation of the Temperature Vegetation Dryness Index (TVDI), highly sensitive to soil moisture deficits in small semi-arid areas, further improved the ADI's performance. Validation of the synthetic Landsat images through statistical metrics (R^2, RMSE, AAD) and visual comparisons confirmed the accuracy and reliability of the reconstructed imagery, ensuring robust drought assessment. The resulting ADI maps consistently revealed persistent drought conditions across the study area between 2014 and 2018, in agreement with established drought indices such as SPI and SPEI. Complementary GRACE-based analyses of hydrological drought in the Iranshahr-Bampur region confirmed declining regional water resources, reinforcing the ADI's capability to capture both short-term agricultural and long-term hydrological drought.

Despite these strengths, continued methodological development and broader evaluation would further enhance the applicability of the proposed framework. Future research should prioritize integrating emerging high-resolution satellite datasets and multi-sensor observations to better capture surface heterogeneity and short-term drought dynamics. Sensitivity analyses are also recommended to quantify fusion uncertainty, LST retrieval errors, and ADI sensitivity as higher-resolution validation data become available. Incorporating ground-based measurements-such as soil moisture, irrigation records, and crop condition data-where available would enable more comprehensive validation and refinement of the index at field and sub-field scales. In addition, extending the framework to diverse agro-climatic regions and cropping systems would allow assessment of its robustness and adaptability under varying environmental and management conditions, supporting its wider use in agricultural drought monitoring.

The high-resolution, multi-variable nature of the combined STI-FM data fusion and the multi-variable ADI provides a high-resolution framework for agricultural drought monitoring in the semi-arid Iranshahr region and supports its potential for operational application to other semi-arid areas following further multi-year testing and uncertainty assessment. For instance, it can be integrated into early-warning systems to support timely interventions in water management and irrigation planning, reducing crop losses and improving food security in semi-arid regions. Policymakers could leverage ADI-derived information to prioritize resource allocation, design targeted drought mitigation strategies, and monitor the effectiveness of agri-environmental programs. Furthermore, by coupling the ADI with socio-economic and crop yield models, the framework could inform risk assessments, insurance schemes, and climate adaptation strategies, bridging the gap between remote sensing research and practical decision-making. Ultimately, this approach offers valuable information to support decision-making, sustainable water resource management, and the enhancement of agricultural resilience under increasing climate change pressures.

Conflict of interest. The Authors do not declare any conflict of interest.

Data Availability Statement: The data presented in this study are available on request from the first author.

7. REFERENCES

Abu Arra, A., Şişman, E., 2024. Innovative Drought Classification Matrix and Acceptable Time Period for Temporal Drought Evaluation. Water Res. Management, 1-23.

Ahrens, C.D., 2015. Meteorology Today: An Introduction to Weather, Climate, and the Environment. Cengage Learning Canada Inc.

Almamalachy, Y.S., Al-Quraishi, A.M.F., Moradkhani, H., 2020. Agricultural drought monitoring over Iraq utilizing MODIS products. In: Environmental Remote Sensing and GIS in Iraq, 253-278. https://doi.org/10.1007/978-3-030-21344-2_11

Atzberger, C., 2013. Advances in remote sensing of agriculture: Context description, existing operational monitoring systems and major information needs. Remote Sensing 5(2), 949-981. https://doi.org/10.3390/rs5020949

Becker-Reshef, I., Justice, C., Sullivan, M., Vermote, E., Tucker, C., Anyamba, A., *et al.*, 2010. Monitoring global croplands with coarse resolution Earth observations: The Global Agriculture Monitoring (GLAM) project. Remote Sensing 2(6), 1589-1609. https://doi.org/10.3390/rs2061589

Carlson, T.N., Gillies, R.R., Perry, E.M., 1994. A method to make use of thermal infrared temperature and NDVI measurements to infer surface soil water content and fractional vegetation cover. Remote Sensing Reviews 9(1-2), 161-173.

Chen, Z., Cai, Y., Liu, Y., Liang, Z., Chen, H., Ma, R., *et al.*, 2025.

Towards end-to-end rice row detection in paddy fields exploiting two-pathway instance segmentation. Computers Electronics Agriculture 231, 109963.

Didan, K., Munoz, A.B., Solano, R., Huete, A., 2015. MODIS Vegetation Index User's Guide (MOD13 Series). University of Arizona, Vegetation Index and Phenology Lab, 35 pp.

Famiglietti, J.S., Lo, M., Ho, S.L., Bethune, J., Anderson, K., Syed, T.H., *et al.*, 2011. Satellites measure recent rates of groundwater depletion in California's Central Valley. Geophysical Res. Letters 38(3). https://doi.org/10.1029/2010GL046442

Feng, M., Huang, C., Channan, S., Vermote, E.F., Masek, J.G., Townshend, J.R., 2012. Quality assessment of Landsat surface reflectance products using MODIS data. Computers Geosciences, 38(1), 9-22. https://doi.org/10.1016/j.cageo.2011.04.011

Fensholt, R., Sandholt, I., 2003. Derivation of a shortwave infrared water stress index from MODIS near-and shortwave infrared data in a semiarid environment. Remote Sensing Environ. 87(1), 111-121.

Fu, D., Chen, B., Wang, J., Zhu, X., Hilker, T., 2013. An improved image fusion approach based on enhanced spatial and temporal adaptive reflectance fusion model. Remote Sensing 5(12), 6346-6360. https://doi.org/10.3390/rs5126346

Gao, B.-C., 1996. NDWI-A normalized difference water index for remote sensing of vegetation liquid water from space. Remote Sensing Environ. 58(3), 257-266.

Gao, F., Masek, J., Schwaller, M., Hall, F., 2006. On the blending of the Landsat and MODIS surface reflectance: Predicting daily Landsat surface reflectance. IEEE Trans. Geosci. Remote Sensing 44(8), 2207-2218. https://doi.org/10.1109/TGRS.2006.872081

Gao, Z., Gao, W., Chang, N.-B., 2011. Integrating temperature vegetation dryness index (TVDI) and regional water stress index (RWSI) for drought assessment with the aid of LANDSAT TM/ETM+ images. Int. J. Appl. Earth Observation Geoinformation 13(3), 495-503.

Gholinia, A., Abbaszadeh, P., 2024. Agricultural drought monitoring: A comparative review of conventional and satellite-based indices. Atmosphere 15(9), 1129. https://doi.org/10.3390/atmos15091129

Goshtasby, A.A., Nikolov, S.G., 2007. Guest editorial: Image fusion: Advances in the state of the art. Information Fusion 8, 114-118. https://doi.org/10.1016/j.inffus.2006.04.001

Hamarash, H., Rasul, A., Hamad, R., 2024. A novel index for agricultural drought measurement: Soil moisture and evapotranspiration revealed drought index (SERDI). Climate 12(12), 209. https://doi.org/10.3390/cli12120209

Han, Y., Li, Z., Huang, C., Zhou, Y., Zong, S., Hao, T., *et al.*, 2020. Monitoring droughts in the Greater Changbai Mountains using multiple remote sensing-based drought indices. Remote Sensing 12(3), 530. https://doi.org/10.3390/rs12030530

Hao, Z., Singh, V.P., Xia, Y., 2018. Seasonal drought prediction: Advances, challenges, and future prospects. Rev.Geophys. 56(1), 108-141. https://doi.org/10.1002/2016RG000549

Hassan, Q.K., Bourque, C.P., Meng, F.R., Cox, R.M., 2007. A wetness index using terrain-corrected surface temperature and normalized difference vegetation index derived from standard MODIS products: An evaluation of its use in a humid forest-dominated region of eastern Canada. Sensors 7, 2028-2048.

Hazaymeh, K., Almagbile, A., 2018. A comparative analysis of spatiotemporal data fusion models for Landsat and MODIS data. Int. Archives of the Photogrammetry, Remote Sensing Spatial Inf. Sci. 42, 491-495. https://doi.org/10.5194/isprs-archives-XLII-3-491-2018

Hazaymeh, K., Hassan, Q.K., 2015. Fusion of MODIS and Landsat-8 surface temperature images: A new approach. PLoS One 10(3), e0117755. https://doi.org/10.1371/journal.pone.0117755

Huang, B., Wang, J., Song, H., Fu, D., Wong, K., 2013. Generating high spatiotemporal resolution land surface temperature for urban heat island monitoring. IEEE Geosci. Remote Sensing Letters 10(5), 1011-1015. https://doi.org/10.1109/LGRS.2012.2227930

Huang, E., Zhu, G., Meng, G., Wang, Y., Chen, L., Miao, Y., *et al.*, 2025. Historical dataset of reservoir construction in arid regions. Scientific Data 12, 1428.

Huang, L.S., Guan, Q.S., Dong, Y.S., Zhang, D.Y., Huang, W.J., Liang, D., 2012. Using temperature vegetation drought index for monitoring drought based on remote sensing data. Advanced Materials Res. 356, 2854-2859.

Jia, J., Wang, Y., Zheng, X., Yuan, L., Li, C., Cen, Y., *et al.*, 2025. Design, performance, and applications of AMMIS: A novel airborne multimodular imaging spectrometer for high-resolution Earth observations. Engineering 47, 38-56.

Jia, J., Zheng, X., Wang, Y., Chen, Y., Karjalainen, M., Dong, S., *et al.*, 2024. The effect of artificial intelligence evolving on hyperspectral imagery with different signal-to-noise ratio, spectral and spatial resolutions. Remote Sensing Environ. 311, 114291.

Jiang, D., Zhuang, D., Huang, Y., Fu, J., 2011. Survey of multispectral image fusion techniques in remote sensing applications. In: Image Fusion and Its Applications 1, 1-22.

Kimura, R., 2007. Estimation of moisture availability over the Liudaogou river basin of the Loess Plateau using new indices with surface temperature. J. Arid Environ. 70(2), 237-252. https://doi.org/10.1016/j.jaridenv.2006.12.021

Kovalskyy, V., Roy, D.P., Zhang, X.Y., Ju, J., 2012. The suitability of multi-temporal web-enabled Landsat data NDVI for phenological monitoring-a comparison with flux tower and MODIS NDVI. Remote Sensing Letters 3(4), 325-334. https://doi.org/10.1080/01431161.2011.593581

Landsat, U., 2014. Product Guide – Using the USGS Landsat 8 Product. USGS, 2016.

Lenczuk, A., Olivera-Guerra, L., Klos, A., Bogusz, J., 2024. On the ability to study regional hydrometeorological changes using GPS and GRACE measurements. Progress in Earth Planetary Sci. 11, 63. https://doi.org/10.1186/s40645-024-00665-4

Lian, Z., Zhan, Y., Zhang, W., Wang, Z., Liu, W., Huang, X., 2025. Recent advances in deep learning-based spatiotemporal fusion methods for remote sensing images. Sensors 25(4), 1093. https://doi.org/10.3390/s25041093

Liao, C., Wang, J., Pritchard, I., Liu, J., Shang, J., 2017. A spatio-temporal data fusion model for generating NDVI time series in heterogeneous regions. Remote Sensing 9(11), 1125. https://doi.org/10.3390/rs9111125

Liu, H., Weng, Q., 2012. Enhancing temporal resolution of satellite imagery for public health studies: A case study of West Nile Virus outbreak in Los Angeles in 2007. Remote Sensing Environ. 117, 57-71. https://doi.org/10.1016/j.rse.2011.06.023

Liu, Q., Zhang, S., Zhang, H., Bai, Y., Zhang, J., 2020. Monitoring drought using composite drought indices based on remote sensing. Sci. Total Environ. 711, 134585. https://doi.org/10.1016/j.scitotenv.2019.134585

Liu, W., Wang, J., Zuo, H., Fu, Z., Xiao, W., Cui, Y., *et al.*, 2025. Spatiotemporal distribution and variation characteristics of convective activities in different climate zones in Northern China based on 25 years of satellite observations. Int. J. Climatology 45, e8908.

Long, D., Yang, Y., Wada, Y., Hong, Y., Liang, W., Chen, Y., *et al.*, 2015. Deriving scaling factors using a global hydrological model to restore GRACE total water storage changes for China's Yangtze River Basin. Remote Sensing Environ. 168, 177-193. https://doi.org/10.1016/j.rse.2015.07.003

Lorenzo-Lacruz, J., Vicente-Serrano, S.M., López-Moreno, J.I., Beguería, S., García-Ruiz, J.M., Cuadrat, J.M., 2010. The impact of droughts and water management on various hydrological systems in the headwaters of the Tagus River (central Spain). J. Hydrology 386(1-4), 13-26. https://doi.org/10.1016/j.jhydrol.2010.01.001

Madadgar, S., Moradkhani, H., 2014. Spatio-temporal drought forecasting within Bayesian networks. J. Hydrology 512, 134-146.

Masek, J.G., Vermote, E.F., Saleous, N.E., Wolfe, R., Hall, F.G., Huemmrich, K.F., *et al.*, 2006. A Landsat surface reflectance dataset for North America, 1990-2000. IEEE Geosci. Remote Sensing Letters 3(1), 68-72. https://doi.org/10.1109/LGRS.2005.857030

McKee, T.B., Doesken, N.J., Kleist, J., 1993. The relationship of drought frequency and duration to time scales. Proc. 8th Conf. Applied Climatology.

McVicar, T.R., Roderick, M.L., Donohue, R.J., Li, L.T., Van Niel, T.G., Thomas, A., *et al.*, 2012. Global review and synthesis of trends in observed terrestrial near-surface wind speeds: Implications for evaporation. J. Hydrology 416, 182-205.

Meng, J., Du, X., Wu, B., 2013. Generation of high spatial and temporal resolution NDVI and its application in crop biomass estimation. Int. J. Digital Earth 6(3), 203-218. https://doi.org/10.1080/17538947.2011.623189

Meng, G., Zhu, G., Jiao, Y., Qiu, D., Wang, Y., Lu, S., *et al.*, 2025a. Soil salinity patterns reveal changes in the water cycle of inland river basins in arid zones. Hydrology Earth System Sci. 29, 5049-5063.

Meng, Q., Chen, S., Zhang, L., Zhu, X., Zhang, Y., Atkinson, P.M., 2025b. GLOSTFM: A global spatiotemporal fusion model integrating multi-source satellite observations to enhance land surface temperature resolution. Remote Sensing Environ. 319, 114640. https://doi.org/10.1016/j.rse.2025.114640

Mishra, A.K., Singh, V.P., 2010. A review of drought concepts. J. Hydrology, 391(1-2), 202-216.

Mliyeh, M.M., Aqnouy, M., Laaraj, M., Bouizrou, I., Tariq, A., Benaabidate, L., *et al.*, 2025. Assessing drought dynamics in a semi-arid basin: A multi-index approach using hydrological and remote-sensing indicators. Environ. Sciences Europe 37, 180. https://doi.org/10.1186/s12302-025-01240-4

Palmer, W.C., 1965. Meteorological drought. U.S. Weather Bureau Research Paper 45, 1-58.

Palmer, W.C., 1968. Keeping track of crop moisture conditions, nationwide: The new crop moisture index. Weatherwise 21(4), 156-161. https://doi.org/10.1080/00431672.1968.9932814

Peng, S., Bao, N., Gu, N., Qian, H., Han, Z., Zhou, B., *et al.*, 2025. Enhanced assessment of chlorophyll-a and total nitrogen dynamics using unmanned aerial vehicle-based model and hyperspectral imagery in coastal wetland water. Environ. Technology Innovation 30, 104521.

Poudel, B., Dahal, D., Banjara, M., Kalra, A., 2024. Assessing meteorological drought patterns and forecasting accuracy with SPI and SPEI using machine learning models. Forecasting 6(4), 1026-1044. https://doi.org/10.3390/forecast6040051

Qian, S., Chen, Y., Wang, W., Zhang, G., Li, L., Hao, Z., *et al.*, 2025. Physics-guided deep neural networks for bathymetric mapping using Sentinel-2 multi-spectral imagery. Frontiers in Marine Science 12, 1636124.

Rahimzadeh-Bajgiran, P., Omasa, K., Shimizu, Y., 2012. Comparative evaluation of the Vegetation Dryness Index (VDI), the Temperature Vegetation Dryness Index (TVDI) and the improved TVDI (iTVDI) for water stress detection in semi-arid regions of Iran. ISPRS J. Photogrammetry Remote Sensing 68, 1-12. https://doi.org/10.1016/j.isprsjprs.2011.10.009

Rahman, K.U., Ejaz, N., Shang, S., Balkhair, K.S., Alghamdi, K.M., Zaman, K., *et al.*, 2024. A robust integrated agricultural drought index under climate and land use variations at the local scale in Pakistan. Agric. Water Manag. 295, 108748. https://doi.org/10.1016/j.agwat.2024.108748

Ren, C., Zhang, X., Tian, J., Li, X., Wang, S., Tang, Z., *et al.*, 2026. GRACE-based hydrological droughts are less frequent but more severe than meteorological droughts in global major basins. J. Hydrology 664, 134582. https://doi.org/10.1016/j.jhydrol.2025.134582

Rocha, J., Perdigão, A., Melo, R., Henriques, C., 2012. Remote sensing based crop coefficients for water management in agriculture. Sustainable Development 167-192.

Rouse, J.W. Jr., Haas, R.H., Schell, J.A., Deering, D.W., 1974. Monitoring the vernal advancement and retrogradation (green wave effect) of natural vegetation. NASA, Washington, DC, USA.

Roy, D.P., Ju, J., Lewis, P., Schaaf, C., Gao, F., Hansen, M., *et al.*, 2008. Multi-temporal MODIS-Landsat data fusion for relative radiometric normalization, gap filling, and prediction of Landsat data. Remote Sensing Environment 112(6), 3112-3130. https://doi.org/10.1016/j.rse.2008.03.009

Roy, D.P., Kovalskyy, V., Zhang, H., Yan, L., Kommareddy, I., 2015. The utility of Landsat data for global long term terrestrial monitoring. In: Remote Sensing Time Series: Revealing Land Surface Dynamics 289-305. Springer. https://doi.org/10.1007/978-3-319-15967-6_14

Sandholt, I., Rasmussen, K., Andersen, J., 2002. A simple interpretation of the surface temperature/vegetation index space for assessment of surface moisture status. Remote Sensing Environment 79(2-3), 213-224.

Sharafi, S., Ghaleni, M.M., 2023. Enhancing drought monitoring and prediction in diverse climates by using composite drought indices. Stochastic Environ. Research Risk Assessment 37, 1-21.

Song, H., Huang, B., 2012. Spatiotemporal satellite image fusion through one-pair image learning. IEEE Trans. Geosci. Remote Sensing 51(4), 1883-1895. https://doi.org/10.1109/TGRS.2012.2213095

Srivastava, P., Pandey, V., Suman, S., Gupta, M., Islam, T., 2016. Available data sets and satellites for terrestrial soil moisture estimation. In: Satellite Soil Moisture Retrieval, 29-44. Elsevier. https://doi.org/10.1016/B978-0-12-803388-3.00002-4

Sun, E., Cui, Y., Liu, P., Yan, J., 2026. A decade of deep learning for remote sensing spatiotemporal fusion: Advances, challenges, and opportunities. Information Fusion 126(B), 103675. https://doi.org/10.1016/j.inffus.2025.103675

Sun, H., Zhao, X., Chen, Y., Gong, A., Yang, J., 2013. A new agricultural drought monitoring index combining MODIS NDWI and day-night land surface temperatures: a case study in China. International J. Remote Sensing 34(24), 8986-9001.

Thomas, A.C., Reager, J.T., Famiglietti, J.S., Rodell, M., 2014. A GRACE-based water storage deficit approach for hydrological drought characterization. Geophysical Research Letters 41, 1537 1545. https://doi.org/10.1002/2014GL059323

Trambauer, P., Maskey, S., Werner, M., Pappenberger, F., Van Beek, L., Uhlenbrook, S., 2014. Identification and simulation of space-time variability of past hydrological drought events in the Limpopo River basin, southern Africa. Hydrology Earth System Sci. 18(8), 2925-2942.

Tucker, C.J., Choudhury, B.J., 1987. Satellite remote sensing of drought conditions. Remote Sensing Environment 23(2), 243-251. https://doi.org/10.1016/0034-4257(87)90040-X

Vicente-Serrano, S.M., Beguería, S., López-Moreno, J.I., 2010. A multiscalar drought index sensitive to global warming: The standardized precipitation evapotranspiration index. J. Climate 23(7), 1696-1718. https://doi.org/10.1175/2009JCLI2909.1

Vicente-Serrano, S.M., Pons-Fernández, X., Cuadrat-Prats, J., 2004. Mapping soil moisture in the central Ebro river valley (northeast Spain) with Landsat and NOAA satellite imagery: a comparison with meteorological data. Int. J. Remote Sensing 25(20), 4325-4350. https://doi.org/10.1080/01431160410001712990

Viet, L.V., Thuy, T.T.T., 2024. Drought sensitivity analysis of meteorological and vegetation indices in Dak Nong, Vietnam. J. Water Climate Change 15(10), 4968-4988. https://doi.org/10.2166/wcc.2024.661

Wang, C., Ma, Z., Sun, P., Yang, R., Zhang, C., 2026. Meta-learning-driven intelligent ensemble approach for robust drought evaluation across China. Atmospheric Res. 329, 108492. https://doi.org/10.1016/j.atmosres.2025.108492

Wang, L., Qu, J.J., 2009. Satellite remote sensing applications for surface soil moisture monitoring: A review. Frontiers of Earth Science in China 3, 237-247. https://doi.org/10.1007/s11707-009-0023-7

Wang, N., Wu, Q., Gui, Y., Hu, Q., Li, W., 2024. Cross-modal segmentation network for winter wheat mapping in complex terrain using remote-sensing multi-temporal images and DEM data. Remote Sensing 16(10), 1775. https://doi.org/10.3390/rs16101775

Wang, S., Mo, X., Hu, S., Liu, S., Liu, Z., 2018. Assessment of droughts and wheat yield loss on the North China Plain with an aggregate drought index (ADI) approach. Ecological Indicators 87, 107-116. https://doi.org/10.1016/j.ecolind.2017.12.047

Wang, Z., Fang, S., Zhang, J., 2023. Spatiotemporal fusion model of remote sensing images combining single-band and multi-band prediction. Remote Sensing 15(20), 4936. https://doi.org/10.3390/rs15204936

Wei, Z., Miao, L., Peng, J., Zhao, T., Meng, L., Lu, H., *et al*., 2024. Bridging spatio-temporal discontinuities in global soil moisture mapping by coupling physics in deep learning. Remote Sensing Environment 313, 114371

Weng, Q., Fu, P., Gao, F., 2014. Generating daily land surface temperature at Landsat resolution by fusing Landsat and MODIS data. Remote Sensing Environment 145, 55-67. https://doi.org/10.1016/j.rse.2014.01.011

Xu, Y., Chen, Y., Yang, J., Zhang, W., Wang, Y., Wei, J., *et al*., 2023. Drought in Shanxi Province based on remote sensing drought index analysis of spatial and temporal variation characteristics. Atmosphere 14(5), 799.

Yang, B., Jing, Z.-L., Zhao, H.-T., 2010. Review of pixel-level image fusion. J. Shanghai Jiaotong University (Science), 15, 6-12. https://doi.org/10.1007/s12204-010-7186-y

Yao, P., Fan, H., Wu, Q., 2025. Optimal drought index selection for soil moisture monitoring at multiple depths in China's agricultural regions. Agriculture 15(4), 423. https://doi.org/10.3390/agriculture15040423

Yu, Y., Renzullo, L.J., McVicar, T.R., Malone, B.P., Tian, S., 2023. Generating daily 100 m resolution land surface temperature estimates continentally using an unbiased spatiotemporal fusion approach. Remote Sensing Environment 297, 113784. https://doi.org/10.1016/j.rse.2023.113784

Yu, X., Guo, X., Wu, Z., 2014. Land surface temperature retrieval from Landsat 8 TIRS-Comparison between radiative transfer equation-based method, split window algorithm and single channel method. Remote Sensing 6(10), 9829-9852. https://doi.org/10.3390/rs6109829

Zarch, M.A.A., Sivakumar, B., Sharma, A., 2015. Assessment of global aridity change. J. Hydrology 520, 300-313.

Zargar, A., Sadiq, R., Naser, B., Khan, F.I., 2011. A review of drought indices. Environmental Reviews 19, 333-349.

Zhang, N., Hong, Y., Qin, Q., Liu, L., 2013. VSDI: a visible and shortwave infrared drought index for monitoring soil and vegetation moisture based on optical remote sensing. Int. J. Remote Sensing 34(13), 4585-4609.

Zhang, X., Friedl, M.A., Schaaf, C.B., Strahler, A.H., Hodges, J.C., Gao, F., *et al*., 2003. Monitoring vegetation phenology using MODIS. Remote Sensing Environment 84(3), 471-475. https://doi.org/10.1016/S0034-4257(02)00135-9

Zhang, Y., 2008. Methods for image fusion quality assessment – a review, comparison and analysis. The International Archives of the Photogrammetry, Remote Sensing Spatial Information Sciences 37(B7), 1101-1109.

Zhang, Y., Wang, Z., Huang, M., Li, M., Zhang, J., Wang, S., 2025. S2DBFT: Spectral-spatial dual-branch fusion transformer for hyperspectral image classification. IEEE Trans. Geosci. Remote Sensing 63, 1-17, Art. no. 5525517. https://doi.org/10.1109/TGRS.2025.3608444

Zhu, X., Chen, J., Gao, F., Chen, X., Masek, J.G., 2010. An enhanced spatial and temporal adaptive reflectance fusion model for complex heterogeneous regions. Remote Sensing Environment 114(11), 2610-2623. https://doi.org/10.1016/j.rse.2010.05.032

Zurita-Milla, R., Kaiser, G., Clevers, J., Schneider, W., Schaepman, M.E., 2009. Downscaling time series of MERIS full resolution data to monitor vegetation seasonal dynamics. Remote Sensing Environment 113(9), 1874-1885. https://doi.org/10.1016/j.rse.2009.04.011